Award number W911NF-17-2-0195

Final Report

Integrated Structural Methods Addressing Army Aviation Life Prediction Challenges in Composites

Andrew Makeev
Professor, Mechanical and Aerospace Engineering
Director, Advanced Materials and Structures Lab
University of Texas Arlington
500 W First St, WH 211, Arlington, Texas 76019
(404)840-2378, (817)272-9448
makeev@uta.edu

Yuri Nikishkov
Senior Research Scientist, Advanced Materials and Structures Lab
University of Texas Arlington
500 W First St, WH 211, Arlington, Texas 76019
(404)563-3773, (817)272-9449
yuri@uta.edu

Cooperative Agreement Manager

Robert Haynes
410-278-2397
robert.a.haynes43.civ@mail.mil

11 September 2020

Technical Summary

The Army and Rotorcraft Industry are facing the Future Vertical Lift (FVL) aviation challenge to replace more than 6,300 military vertical lift aircraft over the next 25-50 years. Accurate analysis and prediction methods would reduce development and procurement risk to FVL. In particular, advanced polymeric composites are playing a major role in designing high-performance and lightweight vertical lift structures. However, uncertain remaining useful life of the composite rotor and airframe structures due to complexity of failure mechanisms and susceptibility to manufacturing irregularities which may be precursors to structural damage impose risks that cannot be mitigated exclusively by time-consuming and costly experimental iterations [1]. Consistent with the Army vision for zero-maintenance platforms, fundamental understanding and models for damage progression are needed to reliably detect damage at early stages and predict progression in complex multi-axial/multi-scale environments. Such models would allow for automatic assessment of the condition of composite structure starting from the factory to structural health monitoring (SHM) based assessment in service. It is worth noting that current state of the art in SHM of composite structures suffers from solution uncertainty or multiplicity of the damage scenarios. Validated structural analysis capturing damage phenomena is essential for developing SHM methodology offering unique solutions.

In order to enable validated structural strength and fatigue predictions for larger and complex composite structures up to components we must capture their manufacturing complexity and variability. It is worth noting that the fidelity of the nondestructive inspection (NDI) needed to quantify the smallest defects that would impact structural performance is key to structural diagnostics of aircraft composite parts. However, the fidelity of the traditional NDI methods such as ultrasonic inspection has not been adequate for assessing the condition of composite parts [1]. Such techniques rely on human factor and are impractical for automation needed for the objectivity in the disposition decisions. AMSL recent work on smaller structural details has been extremely useful in identifying technology gaps and giving us a head start in the development of higher-fidelity NDI technology suitable for large structures. In particular, recent improvement in computing power and advances in X-ray computed tomography (CT) based reconstruction make it possible to develop high-resolution limited-angle (partial) CT technology breaking through the object size limits of X-ray CT and offering the long-sought automation for composite aircraft structures needed by the industry. A focused research effort, starting with the development and demonstration of the algorithms and software required for enabling high-resolution partial CT capability to handle large composite structures, has a strong potential for enabling much needed efficient and accurate NDI products, and improved understanding of the failure mechanisms [1].

In this project, we have significantly advanced NDI inspection based on X-Ray Computed Tomography that is applicable to large composite structures breaking through the object size limitations in X-Ray CT applications by the aerospace industry. In particular, a) we have developed novel X-Ray CT scanning technique, Variable Zoom, that enables increased effective resolution and sharpness of defects in high-aspect ratio composite panels. The novel technique features custom scan trajectory that brings the structure close to the X-Ray source when possible, to improve resolution of defect detection; and algorithms improvements to an industry-standard FDK reconstruction method necessary for the high-quality reconstruction of projections obtained using custom trajectory. Also, b) we have built a prototype device inside our cabinet CT system that allowed us to develop and test new methods for one-sided CT that potentially has no size limitations for tested structures; and c) developed new computational methods to improve quality of defect resolution in one-sided X-Ray CT scans.

Validation of the Variable Zoom technique for accurate dimensional measurements was demonstrated on the phantom models and on the CT scans of objects with measurable features. The estimated dimensions of a drilled hole in Carbon/Epoxy panel and Aluminum wires attached to the panel were in line with those obtained by mechanical measurements. In addition, quantitative assessment of the reconstructed detail sharpness demonstrated increased resolution of the defects by the Variable Zoom technique compared to the conventional CT. Finally, we performed a feasibility study on two composite laminate panels manufactured from different composite material systems and subjected to low-velocity impact loads. Both panels had relatively large thickness-to-width aspect ratio, which is a known challenge for a conventional CT scanning technique. In fact, the conventional CT method was not able to achieve the spatial resolution necessary to clearly differentiate smaller cracks and delaminations due to impact; while Variable Zoom technique was able to reconstruct volumes with higher spatial resolution leading to better sharpness of reconstructed slices, including significantly improved defect resolution in the thickness direction. These results were consistent for both material systems under investigation.

For one-sided CT, we used two different configurations to perform CT scans in an inclined setting to demonstrate detection of planar defects in three dimensions. In the first setup, the rotating table was tilted; while the second setup made use of a rotating wheel device designed under this project to perform a one-sided scan. We have shown that inclined reconstructions using iterative statistical algorithm exhibit less artifacts than the analytical method; demonstrated, for instance, by the estimation of the specimen shape and the visibility of defects from the side views. The quality of the statistical reconstruction was greatly improved by using region-of-interest corrections. In addition to ROI correction, we used an edge-preserving prior, in the form of a hyperbolic Total-Variation penalization term, to constrain the solution and limit the influence of the noise while preserving the visibility of the defects, especially in-plane. Lastly, we implemented a bilateral filter in order to improve the visibility and the sharpness of defects. In the example shown below, bilateral filtering has proven to be an efficient noise reduction technique that at the same time keeps the defects under investigation intact.

The Variable Zoom CT technique developed in this work has significant implications for NDI of materials and structures. On the materials side, this method can address the need in achieving the maximum resolution of a CT system without destroying a test article by cutting a small section that can be placed close enough to the X-ray source for sufficient geometric magnification. There is a similar need for structures that can fit into existing CT system enclosures but are subject to small flaws with critical features in three dimensions that are not recognizable using the conventional scanning techniques. Also, the new method offers additional flexibility towards enabling high-resolution CT for larger structures currently not suitable for microfocus CT systems.

Inspection of a large specimen using inclined architecture remains to be performed and requires equipment, which is not currently available. Meanwhile, modifying the laboratory CT setup to an inclined setting that emulates the prospective large specimen scanning device, allowed us to demonstrate improvements to iterative reconstruction methods that can lead to successful high-resolution one-side inspection of micron-sized defects in large structures.

This Project has been partially funded and all funds have been expended to achieve the technical result including effective reconstruction algorithms and software for reliable high resolution partial CT scanning, breaking through the structural scale limits of the CT technology. As a result of research work under this project, we have published one research paper and submitted second research paper for publication (see below). University of Texas at Arlington has submitted a patent application for the Variable Zoom technique developed under this effort. We have presented numerous presentations on the Variable Zoom technique and perspectives of on-sided CT inspection to the industry, including the NDI community of Boeing Company, executives of Shimadzu Corporation and North Star Imaging, and to representatives of Bruker and Pinnacle X-Ray Systems.

Research Papers

1. Nikishkov Y, Kuksenko D, Makeev A. Variable Zoom technique for X-ray computed tomography. *NDT&E International* 2020;116:102310.

2. Dufour J-E, Nikishkov Y, Makeev A. Inclined Computed Tomography Beyond Laminography: Problems and Solutions. Submitted to *Measurement Science and Technology*, October 2020.

Patent Application

Variable Zoom X-Ray Computed Tomography Method for Composites. Applied for permanent US and international patents, US Patent Application 62913775, October 2020.

High-Fidelity Structural Diagnostics

The main objective of this work is to break through the object size limitations of x-ray computed tomography (CT) to enable accurate structural diagnostics of the Army Aviation relevant structures based on partial CT scanning. CT has proven to be the only 3D industrial NDI which has reliable microfocus resolution and objectivity for automated interpretation of the inspection results (targeting the flaws of known concern including porosity/voids, fiber-waviness, cracks and delaminations.) However, the current microfocus CT technology is based on full scanning (currently 360° around the object) which limits the applicability of the technology to small cross sections. Therefore, CT cannot currently accommodate large structures. The proposed effort will develop effective reconstruction algorithms and software for reliable high-resolution partial CT scanning based on limited range of projection angles (less than 180°) which will break through the structural scale limits of the CT technology. Partial scanning will improve the versatility of CT based structural diagnostics to virtually unlimited object in-plane dimensions and will facilitate the development of game-changing NDI systems.

Micro-CT has demonstrated unprecedented ability for reliable 3D NDI of material structure and adequate objectivity for automated interpretation of the inspection results. The following Figure shows CT reconstruction examples revealing manufacturing irregularities and structural damage in a CH-47 aircraft composite main rotor blade structure.

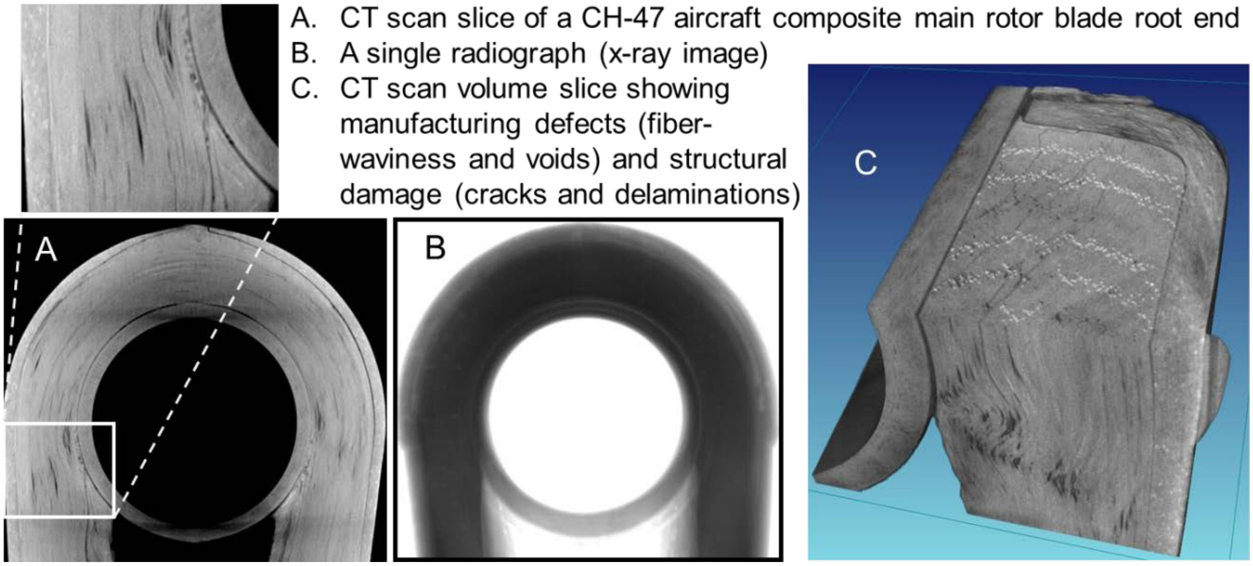

A. CT scan slice of a CH-47 aircraft composite main rotor blade root end
B. A single radiograph (x-ray image)
C. CT scan volume slice showing manufacturing defects (fiber-waviness and voids) and structural damage (cracks and delaminations)

AMSL generated this data under a National Rotorcraft Technology Center / Vertical Lift Consortium Project, Condition-Based Maintenance Technology, a collaborative effort of Boeing, Bell, Sikorsky, UTA, Penn State University, University of Maryland, University of Michigan, and other institutions. While the CT reconstruction from multiple x-ray projections around the composite structure reveals the manufacturing irregularities and structural damage, the single radiograph does not show any meaningful details of the flaws. It is worth noting that locating and characterizing naturally occurring manufacturing defects and structural damage in this composite structure also proved challenging for the other conventional and emerging NDE methods used in that effort.

Furthermore, many existing techniques are subject to human factor and potential errors affecting the objectivity of the inspection and the resulting part disposition decisions. Based on our experience with multiple NDI techniques including x-ray, ultrasound, and thermography-based methods, x-ray computed tomography (CT) has proven to be the only 3D industrial NDE which has reliable resolution up to micron scale depending on the x-ray tube and detector specifications; and adequate objectivity for automated interpretation of the inspection results for advanced composites. AMSL researchers developed a capability to automatically convert CT scan data into 3D structural finite element models for assessment of the effects of the manufacturing defects such as ply-waviness and porosity/voids on structural strength and fatigue performance. It has been determined that small individual voids present at critical locations can significantly reduce strength and durability of composite structure [2, 3].

Perspectives of X-ray CT for Large Structures

An industrial cone-beam CT scan typically includes a series of 2D x-ray images of the object rotating 360º (full scanning). Once the scan is completed, CT reconstruction algorithms are used to generate the 3D volumetric information. It is possible to manipulate the volume in real time and slice anywhere inside the object, after the CT reconstruction. Fourier Transform based analytical filtered backprojection (FBP) software algorithms used in the commercial industrial micro-CT systems are well-suited for efficient reconstruction from full CT scans. However, the ability of such algorithms to reliably reconstruct the details of the inspected object quickly decays as soon as the range of projection angles decreases below 180º. FBP essentially weighs all X-rays equally, and therefore it may not work for many ill-conditioned problems including those with limited-angle projections [4, 5]. The FBP algorithms alone are not suitable for reliable partial (limited angle) scanning. However, we will use the FBP algorithms for initial approximation of limited-angle CT reconstruction and continue with iterative algebraic and stochastic methods to enable reliable microstructural reconstruction from partial scans. .

Unlike frequency-based FBP methods, direct iterative algebraic reconstruction formulations consider the discrete nature of the local x-ray attenuation throughout the material structure without averaging and therefore such methods are better suited for capturing the physics of the local x-ray attenuation throughout the inspected object. There is a mathematical proof that accurate 3D reconstruction can be obtained with algebraic methods from limited range of projection angles with infinite number of projections. The question is in the efficient algorithms and software able to overcome the increased noise levels due to incomplete set of projections in a partial scan. Accordingly, we will approximate the measuring process as a stochastic model with the parameters estimated through a given random sample of the projection values measured by the detector system. The parameters of the stochastic model are treated as random variables following the statistical physics of X-Ray-based measurements; with their distribution representing the x-ray attenuations.

Algebraic and statistical methods for CT image reconstruction require more substantial amount of computational effort compared to FBP. However, the continuously growing computational power of today's standard computers makes the algebraic and statistical reconstruction methods viable for a practical implementation. Now is the right time to start the development of limited-angle industrial CT NDI systems. The novel technology will target the flaws of known concern including porosity/voids, fiber-waviness, cracks and delaminations in large complex structures, and offer a significant improvement over current techniques through maximizing the objectivity of the NDE to a level adequate for the development of fully functional software tools enabling rapid, automated analysis of NDE data for accurate structural diagnostics. It is worth noting that modifying factory X-Ray facilities to allow for partial CT capabilities or designing portable CT devices is relatively easy after developing the effective reconstruction software.

AMSL employed UTA's state-of-the-art micro-focus CT facilities for generating data for the diagnostic technology development and verification. A large customized CT facility, built for UTA by North Star Imaging, Inc. (NSI) can handle structures which are up to 5 feet long. The facility was recently updated with two X-ray detectors bringing state-of-the-art contrast and resolution improvements and dual-tube configuration enabling improved tube focus. In addition, we established a collaborative effort with Shimadzu Corporation that developed custom X-Ray acquisition for Variable Zoom technique in the Shimadzu inspeXio SMX-225CT FPD HR micro-CT system placed at AMSL. The system also features improved detector sensitivity and X-Ray generation for higher contrast and resolution imaging of composite structures.

Reconstruction Methods for Computed Tomography

To advance state-of-the-art in Computed Tomography, it is necessary to implement basic CT reconstruction capabilities. X-Ray CT scan typically obtains between 1,000 to 2,000 radiographs with modern detector providing up to 10 mega-pixel radiographs with 16-bit data depth. These large data sets (up to 50 Gb) represent projections of scanned object from different angles, and possible at different magnifications, depending on scan geometry and trajectory. Since projections are assumed to be proportional to the product of photon field intensity attenuations along each ray, which in turn are approximately proportional to material densities, a computational reconstruction method is needed to obtain densities of a scanned object typically discretized as three-dimensional regular grid of points. Modern high-resolution reconstructions require thousands of discretization points in each dimension, which leads to billions of free variables that are solved for in this inverse problem.

Basics of CT Reconstruction

Reconstruction of the 3D volume from X-ray cone-beam projection radiographs represents a photon transmission tomography problem that has been extensively studied since 1970s. A historical review of the research in the field can be found in [6].

X-ray detector measures intensity of photons attenuated by the material:

$$I = I_0 e^{-\int \mu(x)dx} \tag{1}$$

where I_0 is unattenuated X-ray intensity, μ represents attenuation (that is almost proportional to material density, see [7] for more details on this relationship), and the integral is taken along the line from source to a detector point. Measurements are typically converted to “log” projections, which converts the problem to a linear system of equations.

$$p_i = \log \frac{b}{y_i - r} \tag{2}$$

where y_i is ith radiograph measured by detector, b is detector measurements of X-ray intensity without an object (aka detector gain) and r is detector measurements of zero field (detector offset). In polar coordinates, log-projection is given by:

$$p_\varphi(r) = \int \mu(r', \varphi')\delta[r' \cos(\varphi - \varphi') - r]|r'|dr'd\varphi' \tag{3}$$

where $\delta[\cdot]$ is Dirac’s delta function and p_φ is a projection taken at angle φ. Analytical inverse exists (was first provided in 1917 by Radon [8]) but impractical to implement computationally. Most important theoretical result that gave rise to modern “analytical” reconstruction methods is the Central Slice Theorem, which states that 1D Fourier Transform of projection represents the angular slice of 2D Fourier Transform of solution, i.e.:

$$F[p_\varphi](s) = F[\mu](\mathrm{s}\cos\varphi,\ s\sin\varphi) \tag{4}$$

where F[·] represents Fourier Transform.

Analytical Reconstruction Methods

Reconstruction methods based on Central Slice Theorem are classified as analytical. Analytical reconstruction methods are superior in terms of performance and are used in the majority of commercial medical and industrial X-ray CT systems. Here we describe an analytical reconstruction method developed in this project for the Variable Zoom technique. The algorithm is closely related to the industry-standard Feldkamp–Davis–Kress (FDK) algorithm [9]. In the description of our algorithm below, we follow the presentation of filtered backprojection as convolution-backprojection method as in [10] as this presentation results in highly efficient implementation.

In the first step, X-ray radiographs $P(x, y)$ are weighted to account for different ray lengths in a cone beam to obtain $P'_\theta(x, y_k)$, and convolved with the ramp filter. Radiograph pixel coordinates are defined at the center of rotation, *i.e.* their actual coordinates are divided by the magnification factor to obtain (x, y_k). Then Eq. (5) defines filtered projections:

$$S_\theta(x, y_k) = \left[\frac{P_\theta(x,y_k)}{\sqrt{1+\left(x^2+y_k^2\right)/\mathrm{SOD}(\theta)^2}} * \mathrm{h}(x)\right] \tag{5}$$

An essential step in this reconstruction algorithm is filtering of projections in the frequency domain. In the FDK algorithm a 1D filtering is applied to each row of a weighted 2D radiograph $P'_\theta(x, y_k)$ taken at angle *θ*. In this work we use the following discrete spatial sampling of the ramp filter [10]:

$$h[np_x] = \frac{1}{(2p_x)^2}\begin{cases} 1, & n = 0 \\ 0, & n\ even \\ -1/(\pi n/2)^2, & n\ odd \end{cases} \tag{6}$$

where n is integer $n \in \left[-n_x^{zp}, n_x^{zp}\right), p_x$ is a row pixel spacing, $n_x^{zp} = (2n_x - 1)_2$ rounded to the next power of two, and n_x is the number of pixels in a projection row. The spatial convolution in Eq. 5 is implemented in the frequency domain as follows [28]:

$$[P'_\theta(x, y_k) * \mathrm{h}(x)] = p_x \mathrm{IFFT}\left\{\mathrm{FFT}P'_\theta(x, y_k)_{ZP} \cdot \mathrm{FFT}h[np_x]_{shift}\right\} \tag{7}$$

where FFT / IFFT represent 1D direct and inverse discrete Fourier transform for real input, half-spaces of the filter $h[np_x]$ are swapped using fftshift [11]; and radiographs are zero-padded to n_x^{zp} indicated by subscript *zp* to avoid inter-period artefacts [10].

In the final step, backprojection of a set of filtered radiographs is performed over all projection angles with the additional weighting by w^{vz}:

$$v(t, s, r) = \sum\nolimits_\theta w^{vz}(\theta) z_d^2\,(\theta) S_\theta(xz_d, yz_d) \tag{8}$$

$$z_d(\theta) = \frac{1}{1 - z/SOD(\theta)},\ (x, y, z)^T = R(\theta)R_V \cdot (t, s, r)^T$$

Here $v(t, s, r)$ represents reconstruction volume, R_V is the volume transformation matrix and R_θ is the matrix of specimen rotation. Due to Variable Zoom acquisition trajectory, the "projection" coordinates (x, y, z) are different for each projection angle according to changing SOD. The following weighting factor was found to significantly improve quality of reconstructed through-the-thickness sections:

$$w^{vz}(\theta) = \frac{SOD(\theta)}{SDD} \tag{9}$$

Note that using this weighting factor corresponds to dividing the row pixel spacing p_x in Eqs. (6−7) by the varying magnification factor in Eq. (9).

Variable magnification presents another reconstruction difficulty absent in conventional CT reconstructions. Reconstruction of larger volume than initial ROI, which is only partially visible in the detector, leads to artefacts that correspond to changing effective size of projections. The artefacts are due to the assumption of data periodicity by the Discrete Fourier transform. To eliminate these artifacts, we apply periodic-smooth decomposition [12] to weighted radiographs and use periodic part of radiograph boundary for filtering.

To avoid artifacts at high resolution, reconstruction algorithm must accurately calculate backprojection contributions to voxels over any ray through the object. Discrete application of Eq. (8) involves interpolation of density values from the detector grid to the rotated volume grid. It turns out that "naïve" methods based on the interpolation of projection values or volume coordinates lead to low quality reconstructions. In this work we have implemented two interpolation methods developed specifically for tomographic reconstruction: Distance-driven method [13] and Separable Footprints method [14]. Both methods result in similar results for the presented test cases.

The following describes high-level steps in the implementation of the algorithm:

1. Calculate ramp filter in the frequency domain FFT$h[np_x]_{shift}$ according to Eq. (6);
2. Calculate projection/volume transformation $R(\theta)R_V$ for each projection angle / SOD;
3. Calculate weighted and filtered radiograph $S_\theta(x, y_k)$ using Eqs. (5−7) and applying periodic-smooth decomposition [30] (on the graphics card).
4. Transform volume coordinates using $R(\theta)R_V$ transformation (on the graphics card);
5. Add backprojected pixel values to all voxels as shown in Eq. (8) and using an interpolation method [13−14] (on the graphics card).
6. Repeat starting from Step 2 for all projection angles / SOD.

Iterative Reconstruction Methods

Iterative reconstruction methods are typically based on formulation that is general enough to be applied to any CT system geometry. Iterative methods use both projection of the current reconstruction and backprojection of some form of error to match projections to measured radiographs. The premise of the iterative solution techniques is trying to solve an idealized system:

$$p = Ax + noise \tag{10}$$

Here A is an idealized linear operator of projection such that it converts solution into measurements. The solution is sought in the form of an iterative process:

$$x_{k+1} = x_k + \lambda D^{-1} A^T W (p - A x_k) \tag{11}$$

where x_k is a vector of densities at all volume points (solution sought) at kth iteration, y is a vector of all log-projections at all angles, W is a matrix of algorithm-dependent weights, D is a pre-conditioner matrix (alternatively called update norm) and λ can be a step-dependent convergence rate factor.

Iterative methods can be classified as algebraic, originated from the ART method [15], and statistical methods [16]. Statistical methods, such as maximum likelihood methods, assume radiographs as noisy data and include photon statistics in system modeling [6]. This may result in higher signal-to-noise ratios in reconstructions as compared to analytical methods. In general, all iterative methods can be relatively easily modified to include *a priori* knowledge of the system or reconstructed object. Due to increased number of operations and multiple iterations, iterative methods have been known to require much larger computation times than analytical methods. However, recent achievements, such as ordered subset method [17], and high-performance implementations of projection and backprojection operations have changed this perception.

In this project, we have implemented a) a most commonly used algebraic method, known as SART [18], and b) a statistical method originally as PWLS [19] (renamed to SQS in recent work [20]). Both methods employ ordered subset modification. Using ordered subset method with large number of subsets typically allows to achieve good quality solution in only two iterations. Projection and backprojection operations use Distance-driven method [13] for interpolation between volume and projection spaces.

It can be shown [20] that SART method defines pre-conditioner and weights in Eq. (11) based on purely geometric relationship of projection versus solution space. We use the following update equation by the SART method:

$$x_k^{n+1} = x_k^n + \lambda \frac{M \sum_{i \in S} A_{ik} \frac{p_i - \sum_j A_{ij} x_j^n}{\sum_j A_{ij}}}{\sum_i A_{ik}} \tag{12}$$

Statistical methods attempt to employ additional knowledge based on statistical properties of X-ray measurements. One example is using Poisson’s distribution to correctly capture the statistical effects of low photon counts for high attenuation areas in CT scan [19]. The following update equation is used by the PWLS method:

$$x_k^{n+1} = x_k^n - \lambda \frac{M \sum_{i \in S} A_{ik} w_i \left(\sum_j A_{ij} x_j^n - p_i \right) + \beta Q'_{x_k}(x^n)}{\sum_i A_{ik} w_i \sum_j A_{ij} + \beta Q''_{x_k}(x^n)} \tag{13}$$

In these formulas, A is a linearized system matrix, such that $\sum_j A_{ij} x_j$ is the *i*th line integral, x^n is a reconstructed solution at subset iteration *n*, *p* are logged projections, *M* is number of subsets, *S* is a subset of projections, $w_i = \frac{(Y_i - r_i)^2}{Y_i}$ are PWLS weights for measured projections Y_i, gains b_i

and offsets r_i, such that $p_i = \log \frac{b_i}{Y_i - r_i}$; Q is a convex penalty function in the optimization principle of the PWLS method and β is a damping constant.

High-Performance Implementation

Reconstruction of manufacturing irregularities or structural damage typically requires high resolution volumes with at least hundreds, and preferably thousands of points in each dimension. In the algorithm described above, backprojection is by far the most time-consuming operation during the reconstruction; and its efficient implementation for large volumes must be based on highly parallel computing. In this work we use standard implementation of FFT and IFFT available in modern graphics card hardware and custom backprojection implementation of Eq. (5) that takes advantage of vector processing by implementing computationally intensive interpolation calculations required for each volume point. In addition to per-voxel parallelization, graphics card processors offer multiple command streams that allow concurrent execution of vectorized calculations and memory transfers.

Note that in the implementation of iterative methods, the system matrix A is not explicitly calculated due to its enormous size; instead the sums $\sum_j A_{ij} \cdot$ and $\sum_i A_{ik} \cdot$ are calculated as projection and backprojection operators, respectively. In this work, these operators and iterative updates are implemented in vector-processing hardware available in modern consumer graphics cards, which is used to perform interpolation calculations for each volume point in parallel. Such implementation allows performing iterative reconstructions, *i.e.* 600 1M pixel radiographs to 75M voxel volume and 2 iterations, in about 2 minutes, using a single processor core and single Nvidia 2070 series card. To improve the on-card memory usage, we used number of subsets that was equal to number of radiographs.

Shimadzu inspeXio SMX-225CT FPT HD compute station that has dual 2.3 GHz Intel Xeon E5-2650v3 processor and NVIDIA Quadro M5000 graphics card with 2048 CUDA cores, was used for the reconstructions of the Variable Zoom demonstrations. As an example of performance, the reconstruction from 820 2000×2000-pixel radiographs (about 3.3 billion variables) of a 1329×1266×432 voxel volume (0.7 billion variables) was completed in approximately 7 minutes. The images were cropped from 3000×3000 to 2000×2000 to reduce the amount of redundant information in the radiographs.

Variable Zoom Technique for X-Ray Computed Tomography

Introduction

Despite the advances in CT, high-resolution 3D reconstruction of small defects in objects with large in-plane dimensions remains a fundamental challenge for the X-ray CT-based NDI. Current microfocus CT technology is based on full scanning (currently 360° around the object, or at least 180° plus cone beam angle [6]), which limits the applicability of the technology to small cross sections. Furthermore, even the objects that can be scanned in the existing micro-CT facilities may not allow for sufficient magnification of the composite structure if the resolution requirements place the inspected objects too close to the X-ray tube such that a full scan cannot be completed. Reconstructions using the limited ranges of projection angles below 180° are available in the industrial CT systems, but they often result in inconsistent 3D reconstructions associated with missing projections due to partial access [6, 21].

Extensive research has been undertaken to overcome the size limitations in X-ray CT. Pioneering works emerged in the medical field attempting to reconstruct small-scale regions of interest (ROI) in human bodies, with later expansion to industrial CT. Penßel *et al* investigated modified 360° trajectory for ROI inspection of the partially accessible object [22]. The unconventional scanning trajectory was driven by the size and shape of ROI continuously shifting a specimen as a function of a rotation angle. The findings showed that the proposed trajectory could achieve a high-fidelity scan in the area of interest on simulated 2D phantoms. Dabravolski *et al* used the acquisition trajectory following the convex hull of a specimen [23]. The proposed Adaptive Zooming technique showed a superior reconstruction quality on the artificial data. Maaß *et al* [24] tested several novel approaches combining data from low- and high-resolution scans to improve quality reconstruction. Kyrieleis *et al* [25] have shown that extension of projections is suitable for reasonable approximation of the area of interest where high resolution is not required.

Computed Laminography (CL) is an alternative technique for large objects that cannot be accommodated in an X-ray CT system [26−27]. The technique allows partial access to a test specimen by irradiating an object at an inclined angle. CL has been shown to result in smaller artifacts as compared to limited-angle tomography [28]. Despite the improvement in overcoming geometric constraints related to large in-plane dimensions, CL is not capable to provide the same quality of the out-of-plane defect detection as the full-angle (360°) CT [29−31].

This work presents a new Variable Zoom X-ray CT technique that is targeted to overcome the limitations of large width-to-thickness aspect ratio in cabinet X-ray CT systems and to allow for additional flexibility in achieving high resolution for structures with large in-plane dimensions. The method eliminates the need to destroy the inspection article by cutting out a small section enabling accurate inspection of the composite structure at sufficient magnification. The proposed technique includes two essential aspects: nonconventional radiograph acquisition trajectory and a modification to the industry-standard Feldkamp–Davis–Kress (FDK) reconstruction method that includes weighting of radiographs based on the distance from the panel to the X-ray source and enables higher quality of 3D reconstruction. The analysis of reconstruction quality of CT images produced by the Variable Zoom technique, including dimensional and unsharpness measurements, is carried out on an artificial 3D phantom and on the CT scans of articles with the features of known dimensions. The capability of the method, with the special radiograph acquisition implemented into Shimadzu inspeXio SMX-225CT FPD HR industrial microfocus X-ray CT system, is also demonstrated on the detection of complex structural damage due to low-velocity impact, including accurate detection of through-the-thickness features, in large and thin composite laminate panels, which is among the worst-case scenario for the conventional CT methods.

Scanning Trajectory

Fig. 1 illustrates a cone-beam CT scan setup of a 401-mm Carbon/Epoxy composite laminate panel accommodated inside the Shimadzu X-ray CT system. The panel contains impact damage, which is localized in the central part of the laminate. For conventional CT scan, distance from the X-ray source to the axis of specimen's rotation, known as the source-to-object distance (SOD), remains stationary during the scan. The specimen rotates for a full 360° angular range while being imaged from an X-ray source. Large specimen dimensions prevent necessary magnification of the damaged area that requires high-resolution reconstruction for identification of the defects.

Variable Zoom technique employs an acquisition trajectory with a variable SOD to obtain high-resolution CT scans. The trajectory proposed in this work acquires radiographs with higher geometric magnification by moving the inspected object closer to the X-ray source. The quarter of a proposed scanning trajectory is schematically illustrated in Fig. 2.

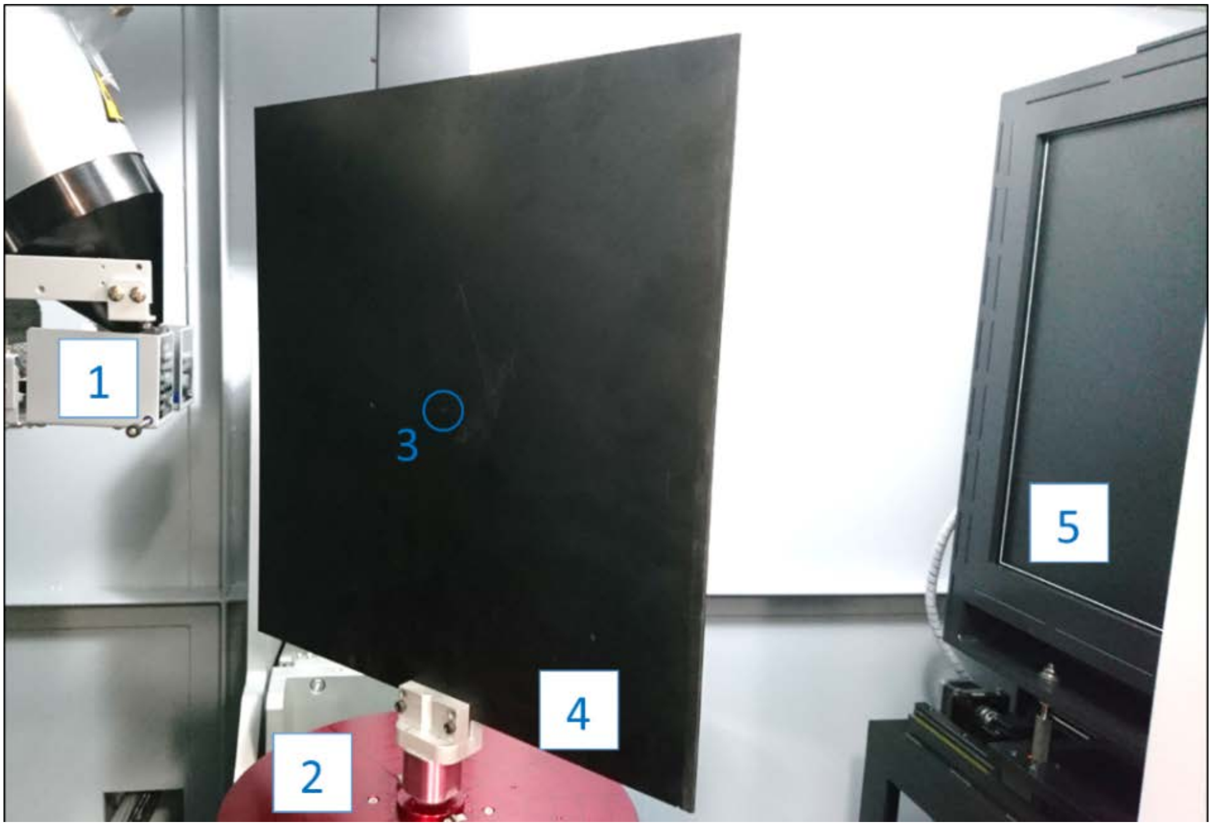

Fig. 1. The Carbon/Epoxy test specimen (4) in the Shimadzu inspeXio SMX-225CT X-ray CT system set at $\theta = 45°$; (1) X-ray tube, (2) turntable, (3) damaged area, and (5) flat panel detector.

Initially, we install a specimen such that the region of interest (ROI) is fully captured in the detector FOV. This distance corresponds to the highest magnification (θ=0°) as illustrated on a top left view in Fig. 2. The scanning trajectory is then defined as:

$$SOD(\theta) = \max\left\{SOD_{ROI},\ S_0 + \frac{1}{2}\left(T_p + (S_p - T_p)|\sin\theta|\right)\right\} \tag{14}$$

where SOD_{ROI} corresponds to the closest distance at which ROI is visible in the detector FOV, S_0 is a safety offset defined by user, S_p is a specimen size, and T_p is a specimen thickness. Note that this trajectory is selected to avoid collision of a specimen with the X-ray tube assuming that the plate cannot go around the source. In this work, we have chosen to keep $SOD(\theta) = SOD_{ROI}$

for $|\theta| < 15°$, while making sure that the ROI stays in the detector FOV for this angular range. Outside of $|\theta| < 15°$ range the specimen moves according to the sinusoidal path defined in Eq. (14) until the SOD reaches maximum at θ=90°. Fig. 2 illustrates only a quarter of the acquisition trajectory, which can be readily extended to 360° range due to symmetry.

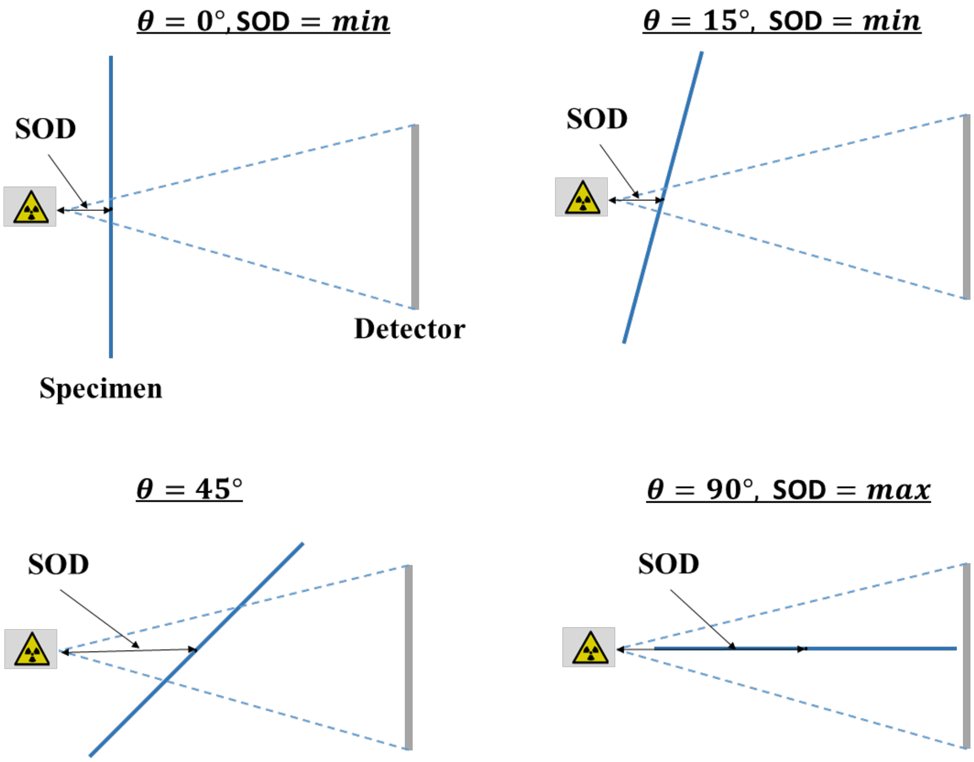

Fig. 2. Variable Zoom acquisition trajectory at 0°, 15°, 45°, and 90°.

Reconstruction Method

Reconstruction is based on a modified industry-standard filtered convolution-backprojection method and incorporates radiograph weighting based on the distance from the panel to the X-ray source. The above section on Analytical Reconstruction describes the method used to reconstruct CT scans with Variable Zoom trajectory. Eq. (9) denotes the necessary modification of the original algorithm as described in [10]. This modification was essential in achieving improved sharpness and resolution of defects in the examples of application of Variable Zoom technique shown below.

Application to High-aspect-ratio Composite Panels

Fig. 3 shows examples of SOD trajectory as a function of specimen rotation angle during the Variable Zoom and conventional CT scans for the large composite panels. In case of the Carbon/Epoxy panel, the SOD remains constant at 265 mm for the conventional CT scan. The SOD for the Variable Zoom trajectory varies from 81 to 265 mm as defined by Eq. (14). Hybrid panel can be accommodated as close as 100 mm using conventional CT scan; and it can move as close as 38 mm when the Variable Zoom trajectory is used.

Shimadzu microfocus X-ray CT cabinet system inspeXio SMX-225CT FPD HR is utilized for all X-ray CT scans. It has a 225kV X-ray tube with a capability to reach 4 µm focal spot size. The system uses high-resolution 16-bit flat panel X-ray detector, 417×417 mm in size, that can acquire up to 3000×3000-pixel radiographs. Distance from the X-ray tube to the flat panel detector, known as the source-to-detector distance (SDD), was set to 800 mm.

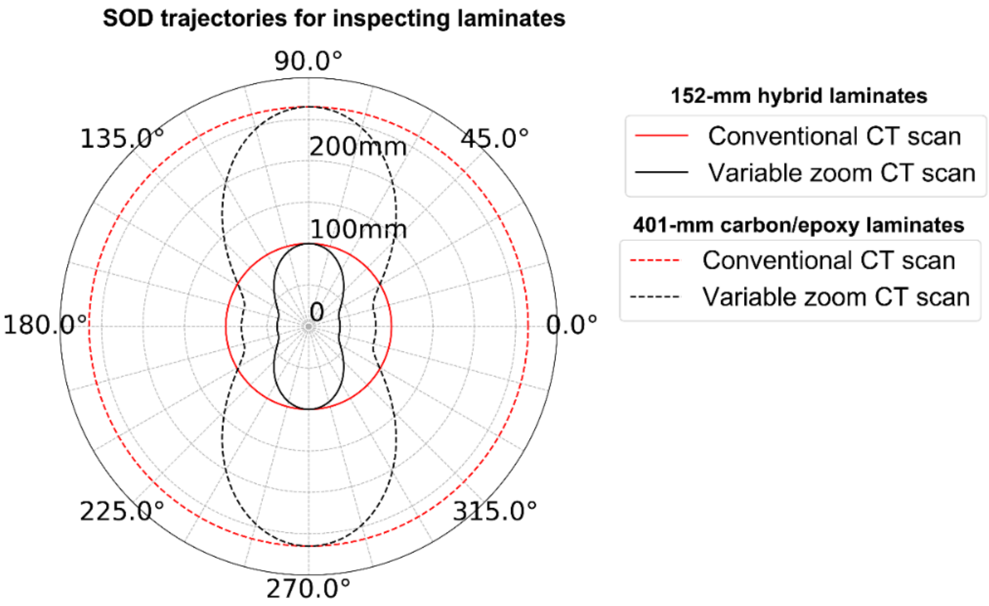

Fig. 3. Comparison of SOD as a function of angular position for the Variable Zoom technique (black) and the conventional CT (red) for 152-mm Hybrid panel and 401-mm Carbon/Epoxy panel.

The Variable Zoom technique is demonstrated on X-ray CT scans of pre-impregnated continuous fiber-reinforced polymer composite panels which have been subjected to low-velocity impact damage. These specimens represent a challenge for the conventional X-ray CT due to large width-to-thickness aspect ratio. Large size of the panels prevents conventional CT scanning techniques from obtaining desired spatial resolution in the area susceptible to damage, which is typically of the size comparable to panel thickness. Reliable defection of interlaminar defects requires reconstruction voxel size to be orders of magnitude smaller than the panel thickness.

Table 1. CT-scan parameters for the Carbon/Epoxy panel and hybrid composite panel.

	401-mm Carbon/Epoxy panel		**150-mm hybrid composite panel**	
	Conventional method	Variable zoom method	Conventional method	Variable zoom method
Tube voltage, kV	180	180	220	220
Target current, µA	90	90	70	70
Magnification	3x	3x-10x	8x	8x-20x
Optimal voxel size, mm	0.046	0.014	0.052	0.021
Angular range, deg	360	210	360	360
Number of projections	1200	820	1200	1200

Detector pixel size, mm	0.139	0.139	0.417	0.417

Each panel has a distinct material system typically encountered in the aerospace applications. The first panel is an IM7-Carbon / 8552-Epoxy composite laminate; and the second panel is a hybrid IM7-Carbon and S2-Glass/913-Epoxy composite laminate. Both panels were manufactured by Boeing using the Hexcel prepregs. Table 1 details CT scan parameters used for evaluation and comparison of the Variable Zoom and conventional CT techniques.

Damage detection in Carbon/Epoxy composite laminate

The first example demonstrates the Variable Zoom technique for the inspection of the impacted area in the Carbon/Epoxy panel. The width and thickness of the panel are 401 mm and 3.5 mm, respectively, resulting in width-to-thickness aspect ratio of 114.57. The panel is subjected to low-velocity impact damage approximately 4×4.5 mm^2 in area located in the middle of the panel.

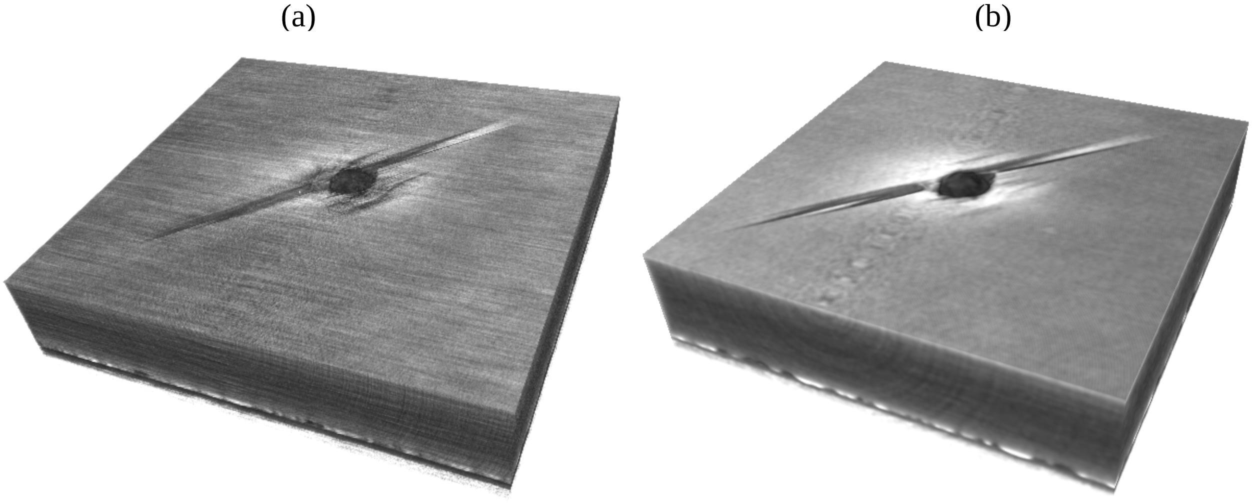

Fig. 4. 3D reconstructed volume of the Carbon/Epoxy panel for: (a) Variable Zoom, (b) conventional method. The conventional scan entails lower resolution; while the Variable Zoom technique produces adequate resolution in all three dimensions.

Fig. 3 illustrates the change in the SOD for conventional and variable zoom trajectories. In the case of conventional scanning trajectory, the SOD remains constant and equals 265 mm resulting in 3X magnification that corresponds to the optimal spatial resolution of 46 μm. The SOD for the Variable Zoom trajectory varies from 81 to 265 mm using the sinusoidal path (Eq. 14), which leads to a maximum 10X magnification for the impacted area in the 401-mm Carbon/Epoxy specimen. The reconstruction voxel size is chosen for the highest magnification and equals 14 μm. We used the 210° angular range (known as short scan) for the Variable Zoom technique to reduce the acquisition time. The orbit was defined by Eq. (1) in the angular range $\theta \in [-105°, 105°]$ and SOD was set to 81 mm for $|\theta| < 15°$.

Fig. 4 illustrates the 3D reconstructed volumes of the Carbon/Epoxy panel. Resolution and sharpness of the volume reconstructed with Variable Zoom technique is superior to the conventional method, although the three-dimensional view makes it difficult to distinguish individual features. The conventional scan entails lower resolution; while the variable zoom technique produces adequate resolution in all three dimensions. Qualitative analysis of reconstruction quality by Variable Zoom technique can be performed by examining slices at different through-the-thickness positions away from the damaged surface area as presented in Fig. 5. The conventional acquisition mode provides images that lack sharpness as can be seen in Fig. 5C−D. Due to inadequate resolution, one cannot discriminate smaller matrix cracks. On the other hand, the Variable Zoom technique increases perceived spatial resolution, and the small size defects can be distinguished as shown in Fig. 5A−B.

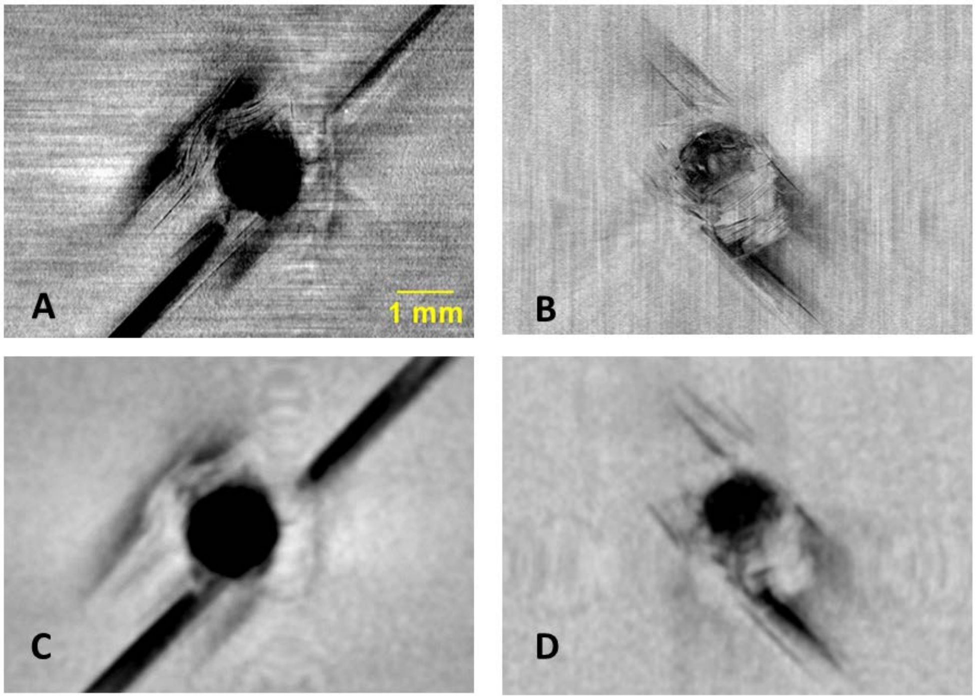

Fig. 5. Slices in planar direction for: (A, B) Variable Zoom; and (C, D) conventional method.

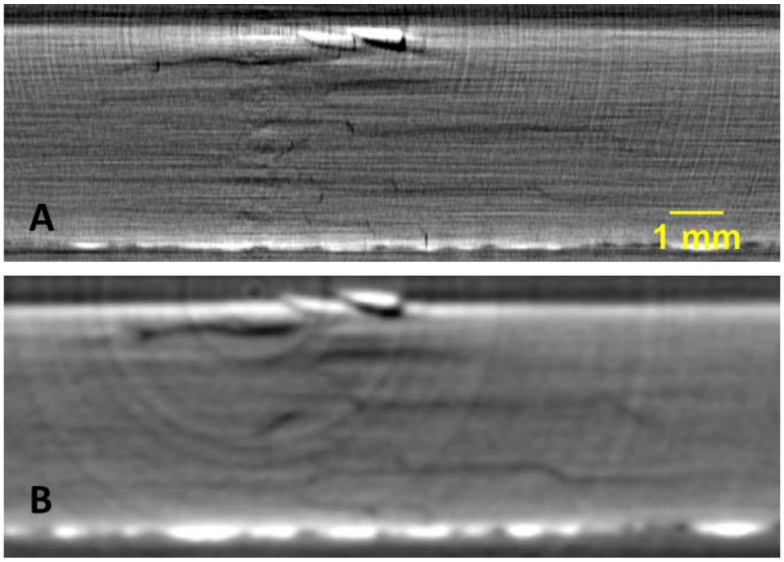

Fig. 6. Slices in through-the-thickness direction for: (A) Variable Zoom, and (B) conventional method.

The same trend emerges by inspecting slices at different depths as illustrated in Fig. 6. Note that the improved sharpness and clarity of delamination reconstruction shown in Fig. 6A by the Variable Zoom technique is truly remarkable. Quality of through-the-thickness slices is strongly affected by lack of angular data leading to the detectable defects appearing smeared through a thickness range. In the spirit of this observation, a zooming technique is expected to improve resolution of planar slices shown in Fig. 6 but not necessarily of the thickness slices. Superior quality of the thickness slices obtained by the Variable Zoom technique is due to the weighting provided by Eq. (9).

Damage detection in hybrid composite laminate

As a second example we applied the Variable Zoom technique to characterize the impact damage in a hybrid composite laminate. This material system imposes additional challenge due to large contrast variation between Carbon and Glass fibers. The laminate has width of 152 mm and thickness of 5.2 mm; the aspect ratio is 29.2; 3×3 mm^2 impact damage is in the center of the plate. The scanning trajectories for this specimen are shown in Fig. 3. The SOD for the conventional acquisition is 100 mm, and the SOD for the Variable Zoom trajectory varies from 38 to 100 mm. Relatively low width-to-thickness ratio of the panel allows achieving 8X magnification; and Variable Zoom technique increases the magnification up to 20X. The reconstruction uses a 360° angular range and a reconstruction voxel size of 21 μm for both techniques.

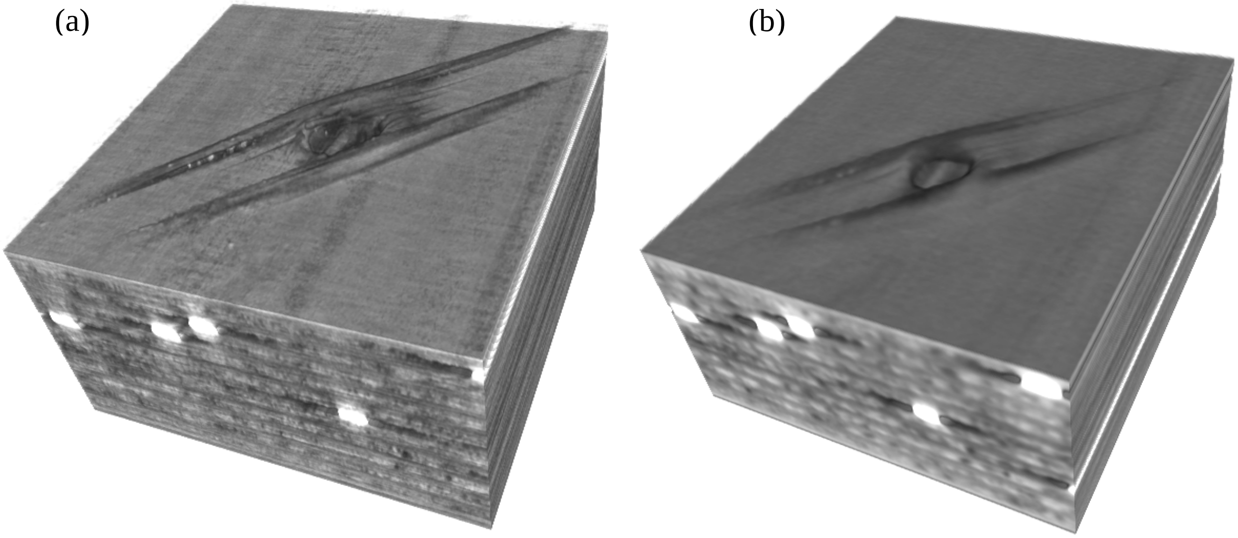

Fig. 7. 3D reconstructed volumes of the 150-mm hybrid specimen for the (a) Variable Zoom; (b) conventional method. Variable Zoom method results in adequate resolution in three dimensions.

Reconstructed volume for the Variable Zoom technique has a superior quality as presented in Fig. 7. The variable zoom method results in adequate resolution in all three dimensions. Again, a clearly improved quality of the through-the-thickness reconstruction slices is not obviously expected and follows from the application of the projection weighting provided by Eq. (9). It is evident that images obtained by the Variable Zoom technique show better sharpness as illustrated in Fig. 8. Despite the relatively high magnification factor used in the conventional acquisition mode, the spatial resolution appears to be inadequate to provide desired reconstruction quality. On the other hand, variable magnification allows achieving higher spatial resolution leading to a better reconstruction quality. Again, note superior sharpness of thickness section reconstructed by the Variable Zoom technique shown in Fig. 8C.

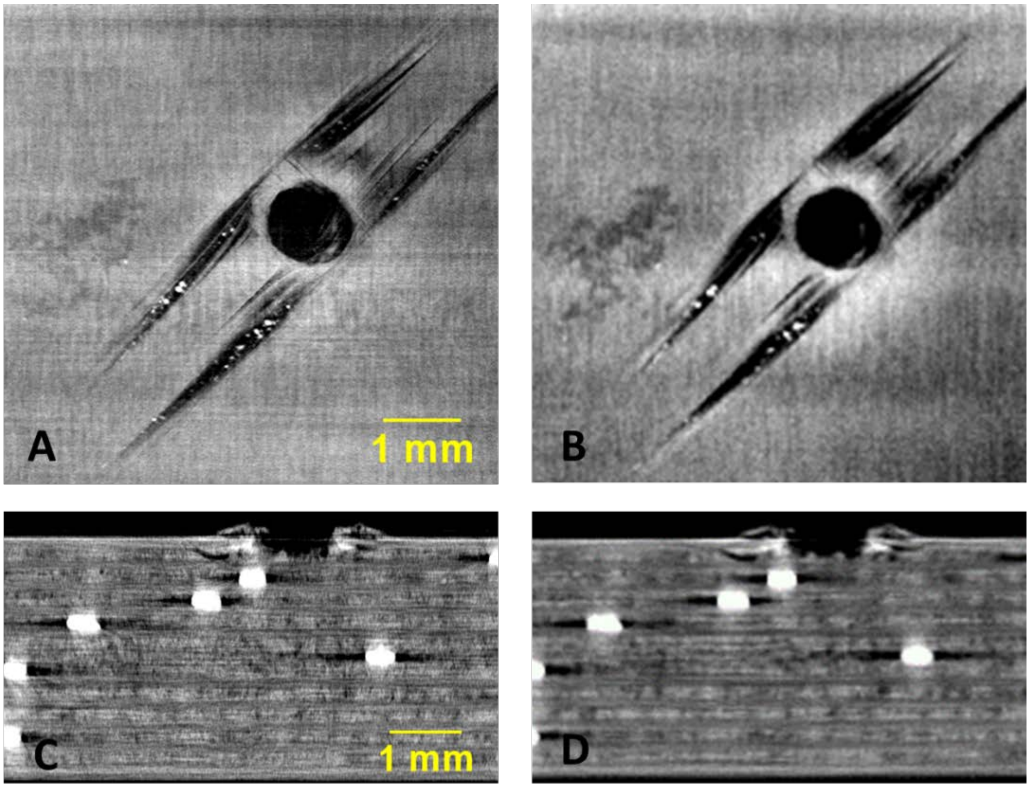

Fig. 8. Slices in planar direction (first row), and through-the-thickness (second row) for: (A, C) Variable Zoom technique, and (B, D) conventional method.

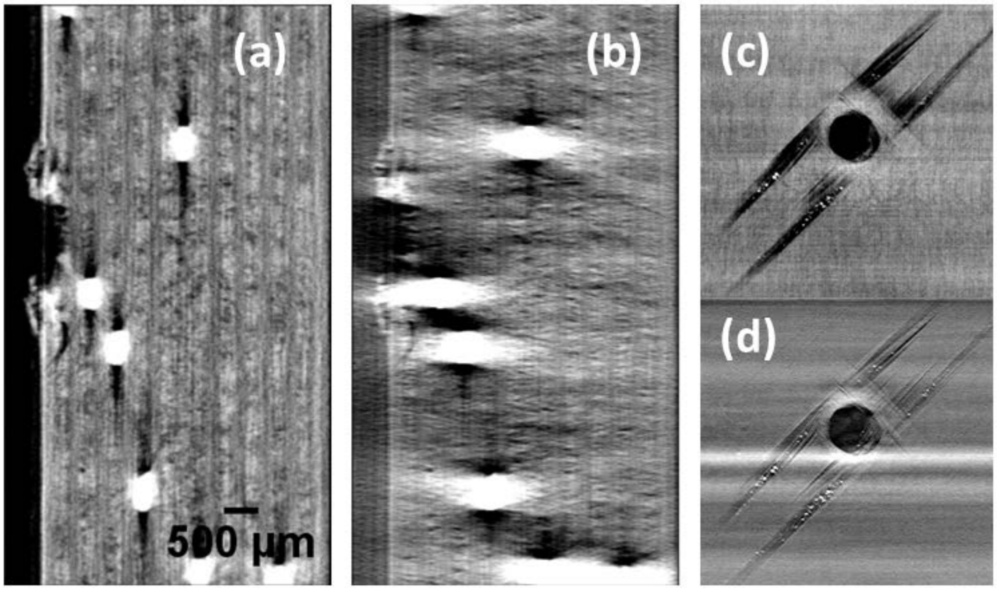

Fig. 9. Slices along the Y-axis (a,b), and along the Z-axis (c,d), Variable Zoom method using weighting in Eq. (4) (a,c), and not using weighting in Eq. (4) (b,d)

Importance of using the weighting factor defined in Eq. (9) cannot be underestimated for the Variable Zoom reconstruction. Fig. 9 provides comparison of Y and Z slices for the Variable Zoom reconstructions that use the weighting factor in Eq. (9) and the reconstructions with no weighting. Fig. 9a shows accurate reconstruction of a through-the-thickness section using Eq. (9). Although the in-plane slices along Z-axis show less noise in Fig. 9d than the same section in Fig. 9c, the Y-axis slices in Fig. 9b show large distortions of features in thickness direction (along Z axis), which is clearly shown by the star patterns from the high-density tracers. Fig. 9d also shows this distortion by the tracer obstruction in the planar section, which is not present in the same section in Fig. 9c.

Phantom-based Evaluation of Variable Zoom Technique

Phantom definition

In this section the performance of the Variable Zoom technique is assessed using an artificial 3D phantom. The phantom volume represents a rectangular 400 mm-wide and 3.5 mm-thick block with a cylindrical defect (0.5 mm in diameter and height) located in the center of the phantom. Dimensions of the phantom mimic the composite panels presented above. The cone-beam projections of a phantom are generated using the projector function [14] and using the geometric parameters and acquisition trajectories for the Carbon/Epoxy panel shown in Fig. 3. To avoid "inverse crime" [32], projections of the phantom volume are generated using a voxel size that is smaller than the one in the projected volume. Due to memory limitations, the full volume is divided in two parts. A smaller inner part with a defect is projected with a 2 µm voxel size and the bigger outer part is generated with 10 µm voxel size. Resulting projections are combined and used as inputs for the analytical reconstruction algorithm developed in this work.

Measurements of defect dimensions

Accurate evaluation of defect dimensions is one of the major criteria in assessing the performance of a nondestructive X-ray CT inspection [7, 33]. In this subsection, we evaluate the accuracy of dimensional measurements (diameter and depth) by the Variable Zoom technique in a phantom and compare it with the conventional CT reconstruction.

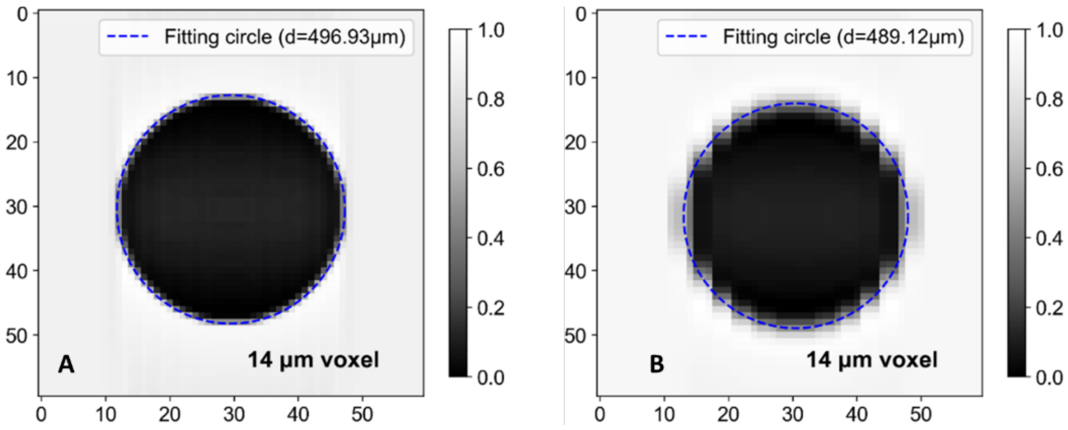

Fig. 10. Estimation of the defect diameter by Variable Zoom technique (A); conventional CT (B).

The diameter of the defect is estimated using a contouring method described in [7]. First, we calculate mean intensity of material and air as shown in Fig. 11. Then, a contour line corresponding to the average material-air value is used to define defect boundary, which is determined with the sub-pixel accuracy. Points along the contour are used to fit a circle, and its diameter is calculated by the least-squares optimization [34] of distances between the points on the contour and their center.

Fig. 10 shows slices of reconstructed volumes in the plane of defects with the defect boundary estimated by the contouring method. Reconstruction by the Variable Zoom technique uses 14-μm voxel size, which corresponds to the highest magnification in Fig. 3, $\theta = 0$ °; and the same reconstruction voxel size is used for the conventional CT method despite lower magnification. The average diameter is estimated using 15 randomly chosen slices. As shown in Table 1, the Variable Zoom technique results in about two times smaller relative error.

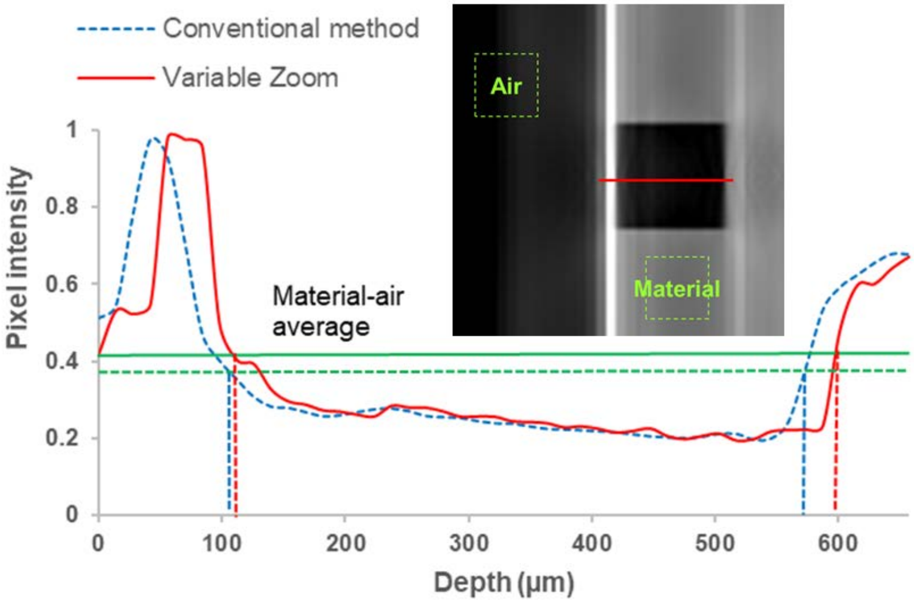

Fig. 11. Defect depth estimation by the line profile tool for conventional method (469 μm) and Variable Zoom (487 μm).

Hole depth is measured using the line profile tool along the defect in the thickness direction. Similar reconstruction slices are chosen for a fair comparison between the methods. The depth of the hole is measured as the length between the two points where the intensity profile intersects the line of the average material-air value. Fig. 11 illustrates depth measurement procedure and compares the line profiles for the Variable Zoom technique and conventional CT. Note that the artifacts that appear as bright strips at the surface of the plate shown in Fig. 11 are present in both reconstructions; they can be attributed to the increased geometric unsharpness of projections that correspond to close approach of the plate edge to the X-ray source shown in Fig. 2, $\theta = 90°$. The Variable Zoom technique demonstrates improvements in accuracy that are similar to diameter measurements.

Measurements of defect sharpness

Visual inspection reveals substantial difference in the sharpness of Variable Zoom and conventional CT reconstruction slices as illustrated, for instance, in Fig. 4. To assess this difference quantitatively, we adopted the variance estimation method proposed in [35]. For each point on the defect boundary, variance of intensity values inside a support window indicates local sharpness of the material-defect boundary. The maximum variance among all measurements along the defect boundary is chosen to represent the sharpness [35].

While ideal for complex boundaries, variance values are difficult to interpret and compare quantitatively. To mitigate this issue, we propose a relationship that estimates the unsharpness of a boundary based on the measured variance. A relationship is established for one-dimensional boundary such that the variance of intensity values along the line profile is related to apparent unsharpness. An assumed intensity profile of the length w across the boundary with unsharpness u is used to calculate the variance for the line profile as illustrated in Fig. 9. Here I_m corresponds to material intensity and I_a to defect / air intensity.

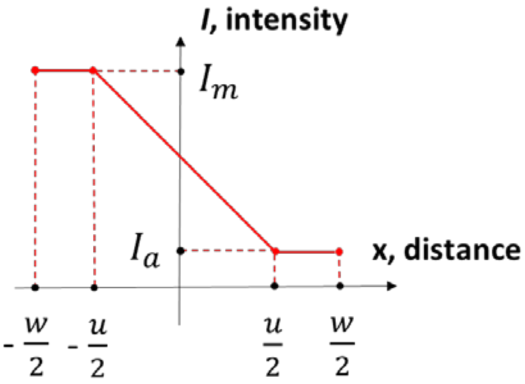

Fig. 12. Normalized intensity profile across the boundary of a defect.

Intensity for the profile shown in Fig. 12 can expressed as a function of a profile coordinate:

$$I(x) = \begin{cases} I_m, x \in [-\frac{w}{2}, -\frac{u}{2}] \\ \frac{I_m+I_a}{2} - \frac{x(I_m-I_a)}{u}, x \in \ [-\frac{u}{2}, \frac{u}{2}] \\ I_a, x \in [\frac{u}{2}, \frac{w}{2}] \end{cases} \tag{15}$$

The variance of intensity for this profile can be calculated and further estimated as:

$$Var = \frac{1}{N}\sum_{k=1}^{N}(I_k - \bar{I})^2 \ \xrightarrow[N\to\infty]{} \ \frac{1}{w}\int_{-w/2}^{w/2}(I(x) - \bar{I})^2 \mathrm{d}x \tag{16}$$

where I_k is the intensity of a pixel and $\bar{I} = \frac{I_m+I_a}{2}$ is the average intensity of the profile.

Substituting Eq. (15) in Eq. (16) and calculating the integral allows expressing the unsharpness u as a function of the variance:

$$u = \frac{3}{2} w\,(1 - Var_n) \tag{17}$$

where $Var_n = \frac{4\,Var}{(I_m - I_a)^2}$ is a normalized variance used in the plots below.

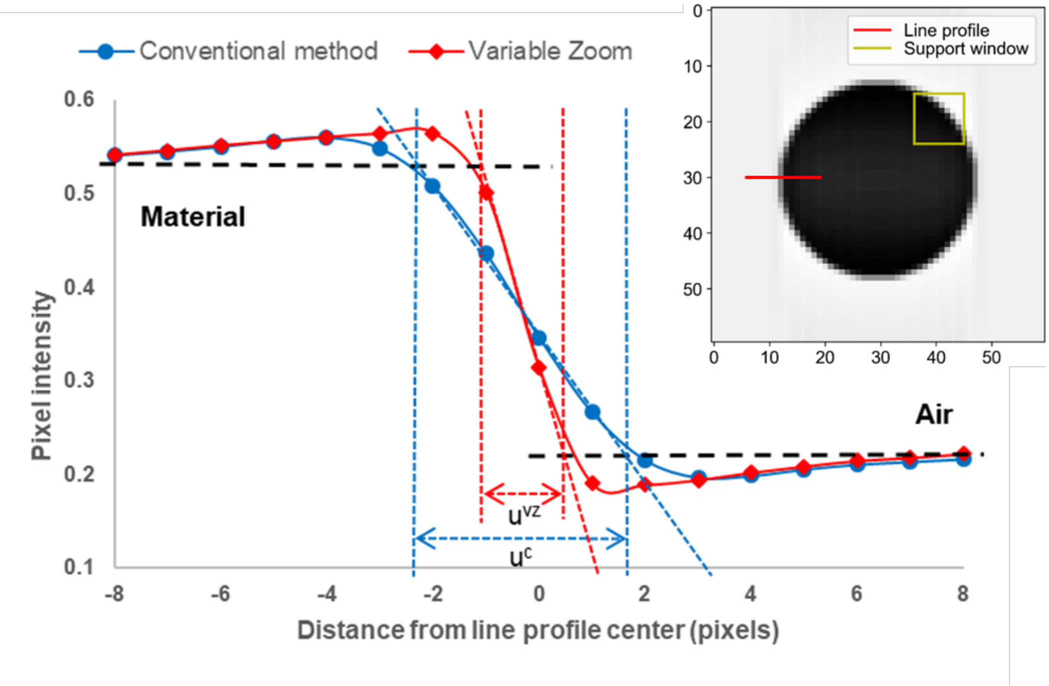

Fig. 13. Estimation of a boundary sharpness based on line profile.

Fig. 13 compares apparent unsharpness of a typical profile for the 500-µm cylindrical void in the 400-mm phantom for both reconstruction methods. A 16-pixel line profile is centered at a point on the material-air boundary defined above. Note that material / air intensities are averaged over large sections away from the boundary. Due to a reconstruction artifact that increases pixel intensity at the material side and decreases it at the air side, the apparent unsharpness is measured as a distance between the intersections of the slope line with the average material / air levels. Fig. 13 shows that the apparent unsharpness u^{vz} for Variable Zoom is almost three times smaller than the unsharpness u^c for the conventional method.

Fig. 14 demonstrates the normalized variance calculated from a discrete form of Eq. (16) and the unsharpness from Eq. (17) as a function of window size. A $w{\times}w$-pixel support window is used for each point on the contour of a hole to obtain maximum variance for the slice. Similar to Fig. 13, to avoid overestimation of the unsharpness due to the boundary artifact, intensity values in the window are clamped to the average material intensity from above and to average air intensity from below. This correction removes the effects of boundary artifacts so that the measured profiles follow the profile in Fig. 12 and Eq. (17) can be used for calculation of the unsharpness. Measurements were performed on 20 sections along the depth of the hole and the error bars indicate standard deviations. As expected, maximum normalized variance of a contour grows almost linearly with respect to window size, while the calculated boundary unsharpness stabilizes after growth at small window sizes. Comparison with Fig. 13 confirms the accuracy of estimating unsharpness based on variance as Fig. 14 shows similar ratio of the unsharpness values for the two methods. Additionally, note that for all windows sizes, the Variable Zoom technique consistently delivers superior sharpness of reconstruction as compared to the conventional method.

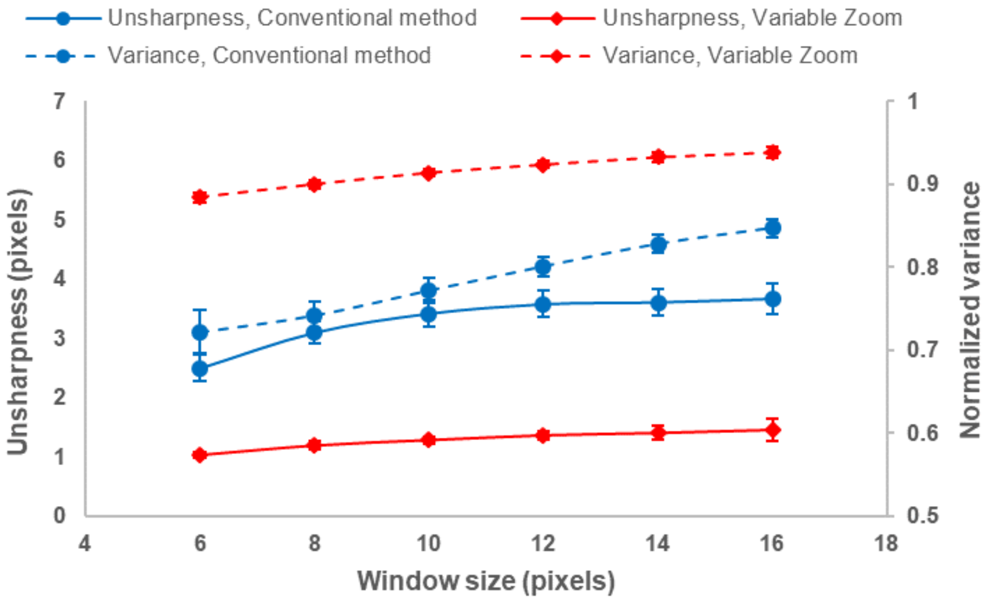

Fig. 14. Phantom boundary unsharpness and normalized variance as function of window size.

Effect of the panel size on the dimensional measurements

This subsection investigates the influence of the panel planar dimensions on defect size and sharpness estimations using the phantom reconstruction. The size of the panel varies from 10 to 400 mm to capture changes in reconstruction quality. Same magnification and reconstruction voxel size were used for this comparison. Simulated scanning trajectories are the same for both methods as outlined in Fig. 3.

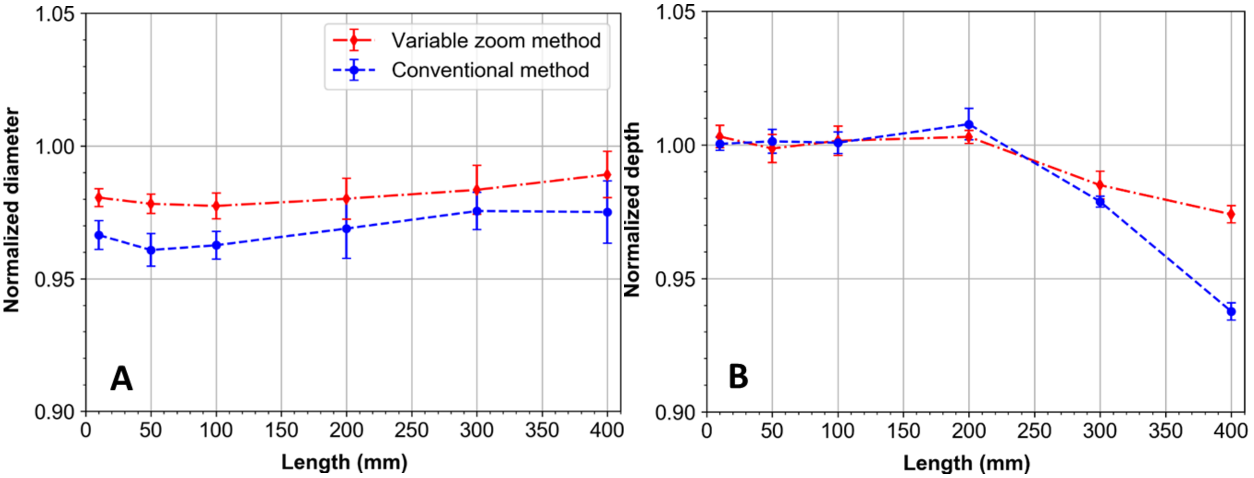

Fig. 15. Dependence of dimensional measurements for defect diameter (A), and depth (B) from the panel size for phantom reconstructions.

Fig. 15 demonstrates dependence of dimensional measurements for defect diameter and depth from the panel size. First, it can be observed that changes in panel size have little effects on diameter and sharpness measurements for both methods but for both measurements the Variable Zoom technique outperforms conventional CT. Second, increase in panel size leads to a decrease in the accuracy of depth measurements as illustrated in Fig. 15B with Variable Zoom technique again outperforming conventional CT. And third, panel size does not appear to affect the boundary unsharpness calculated using Eq. (17) from measured variance in Eq. (16).

Measurement-based Validation of Variable Zoom Technique

Dimensional measurements in a composite panel

Measurement-based validation was carried out on a large aspect ratio Carbon/Epoxy composite panel shown in Fig. 1 manufactured by Boeing using the Hexcel prepreg. A 0.5-mm hole was drilled in the middle of the panel, and the hole’s diameter was confirmed by the Keyence Digital Microscope VHX-950F. The depth of the defect was 2.5 mm, which was estimated by a dial test indicator with 0.001 in (25.4 µm) precision. The dimensional measurements as well as the unsharpness measurements were performed using the procedures outlined in the previous section.

CT scans of the panel were generated using180 kV X-ray tube voltage, 90 µA target current, and 1 frame/sec acquisition speed. 720 3000x3000 radiographs were acquired in a 360-degree angular range. Magnification factor equals 3x for the conventional CT (46 µm optimal voxel size) and varies in 3x-10x range for the Variable Zoom technique. The reconstructions were completed using voxel resolution of 14 µm that corresponds to the maximum magnification factor of 10x. Diameter estimation included 20 hole sections using the methodology illustrated in Fig. 10. Depth measurements have been accomplished using the line profile tool as shown in Fig. 11.

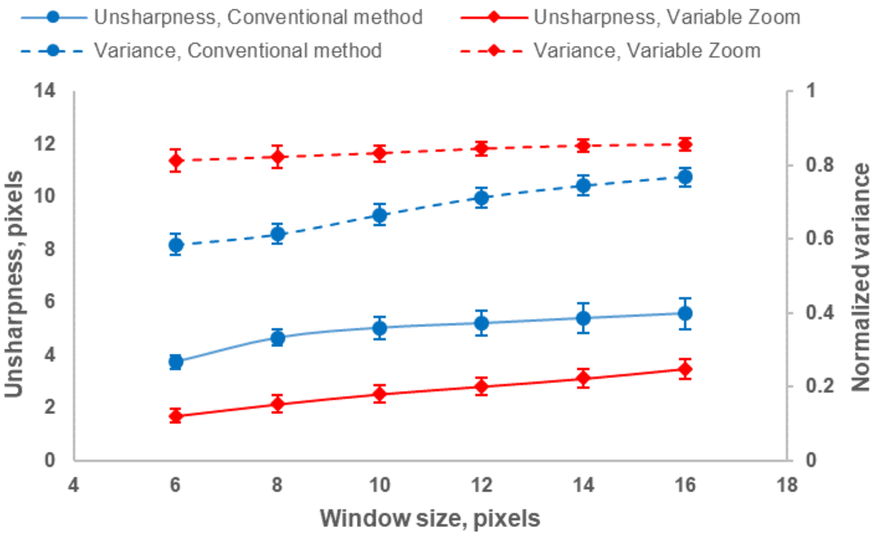

Fig. 16. Drilled hole boundary unsharpness and normalized variance as function of window size.

Dimensional measurements shown in Table 2 indicate that the Variable Zoom technique provides accurate estimation of defect dimensions for an X-ray CT scan performed on a 400-mm composite panel. The difference of the measurements between the phantom and panel CT reconstructions can be attributed to noise in radiographs absent in the phantom.

Fig. 16 provides the normalized variance measurements and unsharpness calculations for 20 sections of drilled hole in the Carbon/Epoxy composite panel. It is evident the Variable Zoom technique results in better sharpness than the conventional CT. Both methods exhibit higher unsharpness values as compared to phantom due to the presence of noise in the radiographs.

Dimensional measurements using Image Quality Indicators

The accuracy of dimensional measurements for the Variable Zoom technique is further assessed using the EN 462-1 image quality indicator (IQI). The IQI is a set of 7 aluminum wires ranging from 0.05 to 0.2 mm in diameter. Two wires, 50 and 100 μm, were extracted from a sealed package and attached to a 400-mm Carbon/Epoxy panel. The diameter of each wire was confirmed with Keyence Digital Microscope VHX-950F.

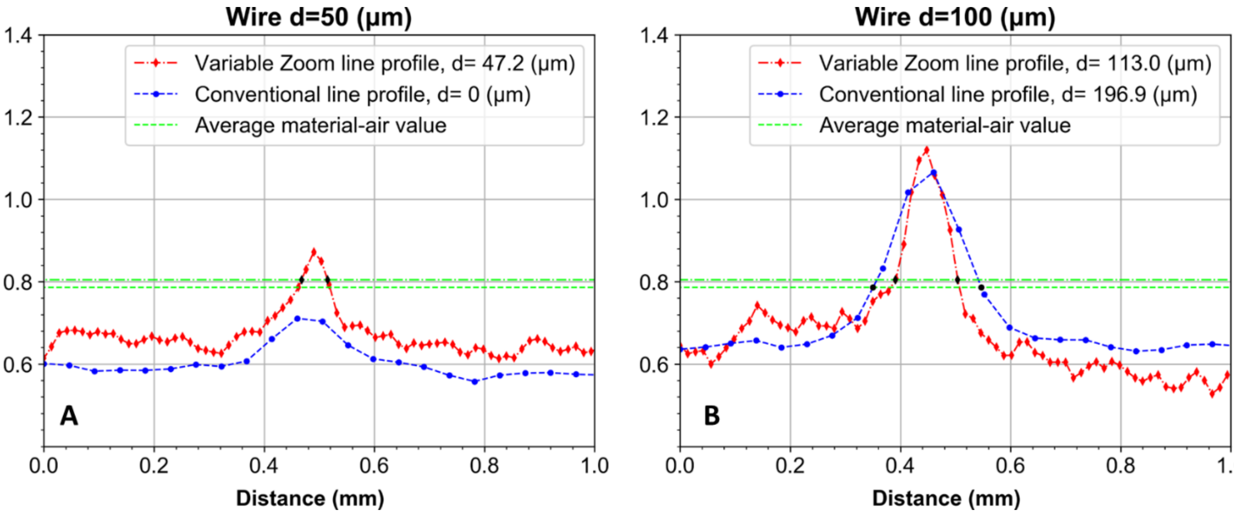

Fig. 17. Comparison of the line profiles for the reconstructions of 50 and 100 μm aluminum wires.

The 50 μm wire poses a challenge for the conventional CT method since the optimal voxel size for the panel is 46 μm, and due to streaking artifacts resulting from large difference in attenuation coefficients between the Aluminum and Carbon/Epoxy. To reduce the artifacts, we used a 0.5 mm-thick Cu filter, 225 kV tube voltage and 120 μA target current. We evaluated diameter of each wire from line profiles across the wire by measuring the distance between the profile intersections with the average material-defect intensity level [7] calculated for each reconstructed 3D volume. Thickness of each wire was measured by averaging 15 line profiles. Fig. 17 shows sample measurements for the 50 and 100-μm wires using the line profile tool.

Table 2 reports the average values and standard deviations of measured wire thicknesses. Note that the thickness of the 50-μm wire cannot be found for the conventional CT method since its line profile did not reach the material-defect average. The measured value of the 100-μm wire thickness for the same method overestimates the nominal thickness of the wire by factor of 2.

The inaccuracy of these measurements results from a combination of a low magnification and streaking artifacts. Table 2 confirms that Variable Zoom method provided more accurate measurements of both 50 and 100-µm wires.

Table 2. Comparison of dimensional measurements.

	Variable Zoom		Conventional CT	
	Average, µm	Relative error, %	Average, µm	Relative error, %
<u>Phantom, hole</u>				
Diameter	496.0±3.0	0.8	488.5±2.6	2.3
Depth	487.0±1.6	2.6	468.8±1.7	6.2
<u>Composite panel, drilled hole</u>				
Diameter	504.32±3.01	0.9	514.69±2.31	2.9
Depth	2454	1.8	2480	0.8
<u>Composite panel, wire attached</u>				
50-µm wire	53±11	6	0	–
100-µm wire	117±13	17	205±16	105

Sharpness Measurement in High-Aspect-Ratio Composite Panels

To quantify differences in sharpness between the two methods we present the analysis of CT slices using variance estimation method described above. The boundaries of defects in both planar and thickness directions were identified by the contouring method [7]. Ten slices adjacent to slices shown in Figs. 5–6 were used to find maximum of local variance measurements for each point on the contour.

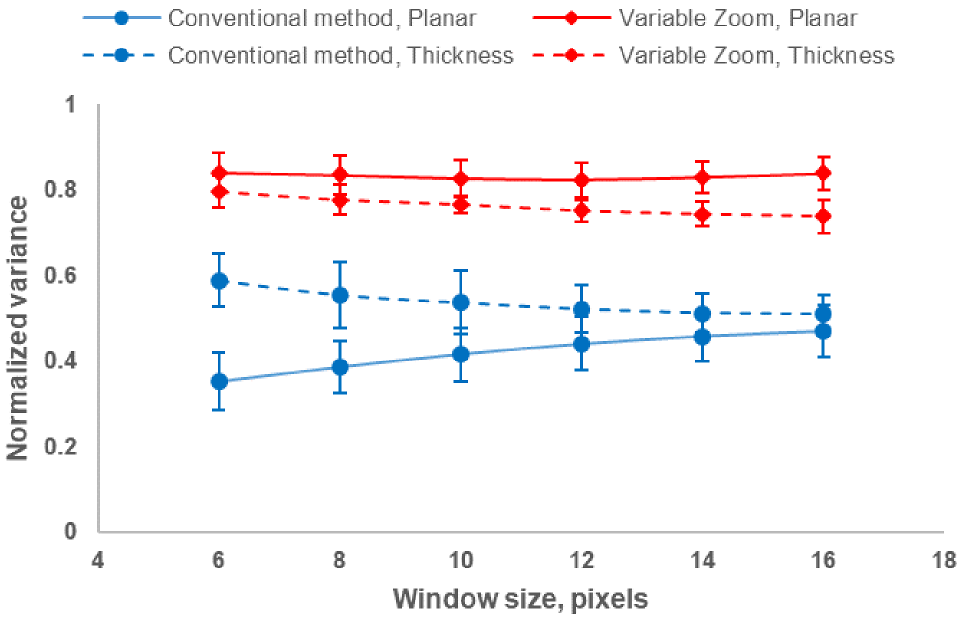

Fig. 18. Boundary unsharpness and normalized variance of impact defects.

Due to extreme complexity of defect boundaries, bigger windows include bigger percentage of boundary pixels than smaller windows, which leads to slower variance growth and increasing unsharpness estimations for bigger window sizes. Therefore, a comparison of variance values is more meaningful for complex defects. Fig. 18 shows normalized variance measurements for Variable Zoom and conventional CT reconstructions that use the same voxel size of 14 µm. Higher variance values for both planar and thickness direction slices by Variable Zoom indicate lower unsharpness of the reconstructed defects. For example, normalized variance of Variable Zoom planar sections $Var_n = 0.83$ corresponds to the unsharpness of 2.6 pixels for window size $w = 10$, while the unsharpness for conventional method is 8.8 pixels. Fig. 18 clearly indicates that Variable Zoom technique provides sharper resolution of defects than the conventional CT.

Inclined Computed Tomography: Solutions for One-Sided CT

Introduction

Computed Laminography (CL) has become an established non-destructive evaluation technique, with a number of commercial systems available for customers, typically used for efficient quality control. CL does not require obtaining radiographs from all directions to obtain useful reconstructions, thus removing the geometric constraints for larger specimens that would otherwise lead to low resolutions [36]. Initially evolved from the classical laminography, CL has become a practical tool for identification of defects in circuit boards due to its ability to achieve high resolution in plane of the specimen while enabling some degree of separation for stacked defects [36]. While [30] identifies all reconstructions from limited data that use various detector / specimen trajectories as laminography, we consider CL as a limited data technique that targets high geometric magnification of a relatively small area of the specimen, low defocusing of the beam available in X-ray transmission tubes, and moderate oblique angles provided by the detector motion. In the authors opinion, this definition is consistent both with the name of laminography that means “to describe thin layer” and practical usage of this technique. For typically stationary X-ray source, CL requires physical movement of the specimen under investigation to maintain an area of interest in the filed-of-view of moving detector.

While being an efficient NDI solution for circuit boards and thin-layered structures, CL is not designed for identification of defects in thicker or larger structures especially if is it difficult or undesirable to rotate or even move them. On the other hand, an older concept of tomosynthesis, a technique that targets low magnification of a stationary specimen and relatively small oblique angles, is capable of only low-resolution reconstructions of planar features. Both of these methods are not well suited for evaluation of three-dimensional (3D) structural details, such as, for example, a complex pattern of cracks resulting from the impact damage in a composite laminate.

This work‘s emphasis is to study 3D reconstructions of more inclusive variety of large structures based on one-sided X-ray inspection using the X-ray system geometry that we identify as Inclined CT. In this concept we combine relatively large oblique angles of the specimen (or the source) with moderate magnification of a specimen that is potentially very large in planar dimensions and not necessarily small in thickness. The goal of this setup is to demonstrate improved shape and defect resolution in three dimensions including side views. One example of such setup is tilting of the axis of rotation in an X-ray cabinet system (referred in [30] as Rotary CL), which still imposes limits on specimen dimensions, proposed in [37] and referred as CLARA. The cabinet system setup was demonstrated in [27] and needed complex 3D corrections and hours-long reconstructions for average-sized volumes. Another cabinet system using fast linear motion scans of composite samples based on the robotic arm was reported in [31] and has shown promising results compared to limited angle scans. More realistic examples involved a robotic arm-driven X-ray source and detector rotating at moderate oblique angles [38] and providing one-sided low-magnification inspection of auto parts [39]. However, these works investigated inspection of details only in the plane of the specimen, perpendicular to the rotation axis, which produces best results in CL. In this work, we show that large oblique angles characteristic to Inclined CT can result in accurate detection of defects in all planes of the reconstruction. The ultimate goal of the Inclined CT is a high-resolution inspection of extremely large planar specimens (such as full-sized helicopter blade and or an airplane wing) based on a stationary device, in which a sample is fixed on the supports, and both X-ray source and detector are rotated and positioned independently with high precision. This configuration will not impose any limits on the planar size of the specimen while providing 3D high-resolution one-sided X-ray inspection. Such device is currently under construction at the University of Texas at Arlington.

It is worth noting that the X-ray inspection of specimens with large in-plane dimensions is not free of artifacts and reconstruction problems even with full angular data available. In the Inclined CT scanning, while the sheer quantity of data may still remain the same, its spread and localization is limited. X-ray scanning from one side imposes limits on the availability of planes within a reconstructed volume perpendicular to rays from the source, which results in additional artifacts typically propagating from the density jumps (i.e. material boundaries) [40]. In planar sections, these artifacts appear as defocused images of boundaries present in different sections; and in thickness sections they often appear as boundary traces dominating the signal. Finally, some defects, such as wide and thin openings in the thickness direction of a specimen, may not be detectable by any reconstruction algorithm [41].

This work provides an assessment of typical problems encountered in Inclined CT scans and discusses their solutions. These problems include reconstruction of region of interest (ROI) from a set of radiographs that contain projected material outside of the FOV; and artifacts specific to Inclined CT reconstructions due to limited data. We also discuss observability of defect measurement in thick specimens targeting both in-plane and out-of-plane defects. Inclined CT reconstructions are investigated using computational phantoms and physical samples using a) tilted axis of rotation setup, and b) a “wheel” device designed by authors that changes the rotation axis of a specimen. We consider both analytical and iterative reconstruction algorithms, noting that iterative algorithms are flexible to provide accurate account of the non-standard system geometry, with high-performance implementation enabling fast average-sized reconstructions in minutes time, not hours as reported in [27].

Inclined CT Geometry

In the most common CT setup, the rotating table supporting the specimen is located between stationary detector and X-ray source as shown in Fig. 19. The specimen is then rotated around the table axis aligned with the vertical direction of the detector.

As mentioned previously, this architecture is not suitable for large structures where rotation of the specimen is impossible. One possible solution is rotation of the source and the detector around the specimen in a concerted motion so that projected region of interest stays within the detector. This technique is commonly used [2] for planar objects in laminography systems. To replicate the scanning trajectories in the existing cabinet CT in order to conduct a feasibility study, we had to settle for the closest approximation possible and smaller samples.

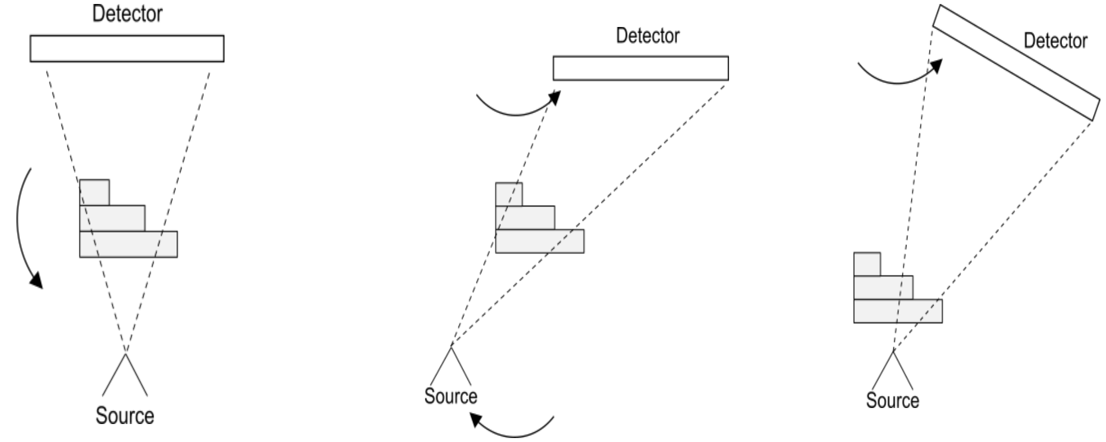

Fig. 19. Schematic of a typical CT setup (left); Inclined CT setup (center); and CL setup (right).

When the rotation of the specimen is possible, inclined CT setup equivalent to the one illustrated in Fig. 19 can be used in a cabinet system as shown in Fig. 20. By inclining the rotating table, it is possible to emulate the Inclined CT setup with some limitations while keeping a sufficiently large zoom factor [27]. Only large tilt angles can be achieved using this setup as the table cannot be tilted more than 25° in our system. Moreover, due to the space limitation inside a CT cabinet, the support handling the specimen and the table could enter the field of view if we were to use larger angles.

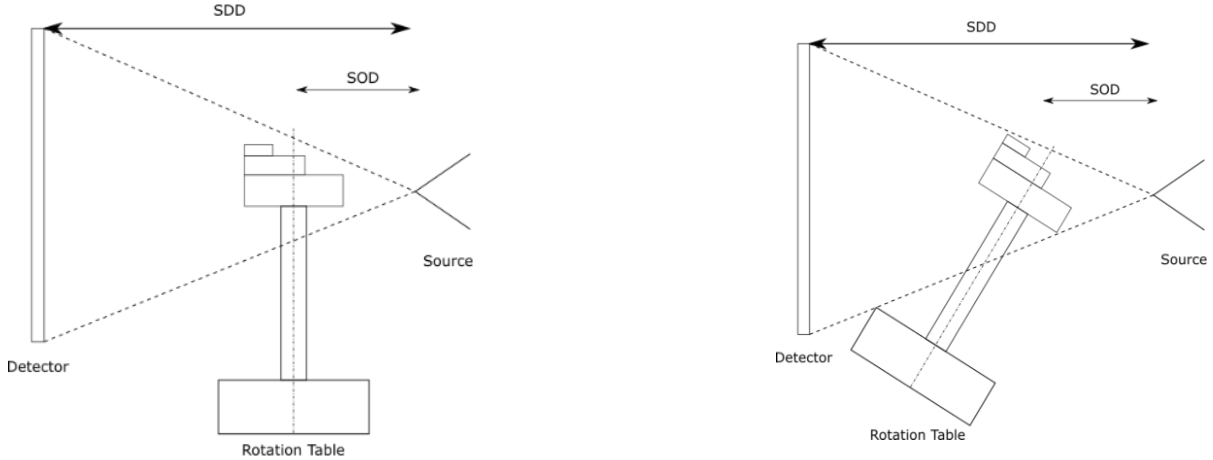

Fig. 20. Comparison between standard CT (left); and inclined table setup (right) side views.

Another possibility to achieve the inclined setup is to use a device changing the axis of rotation of the specimen from the vertical direction to the source-detector direction. The general setup and an example of such a device is shown in Fig. 21. Using this setup allows to incline the specimen by a small tilt angle (as opposed to tilting the rotation table) because the wheel enter the field of views when using larger angles.

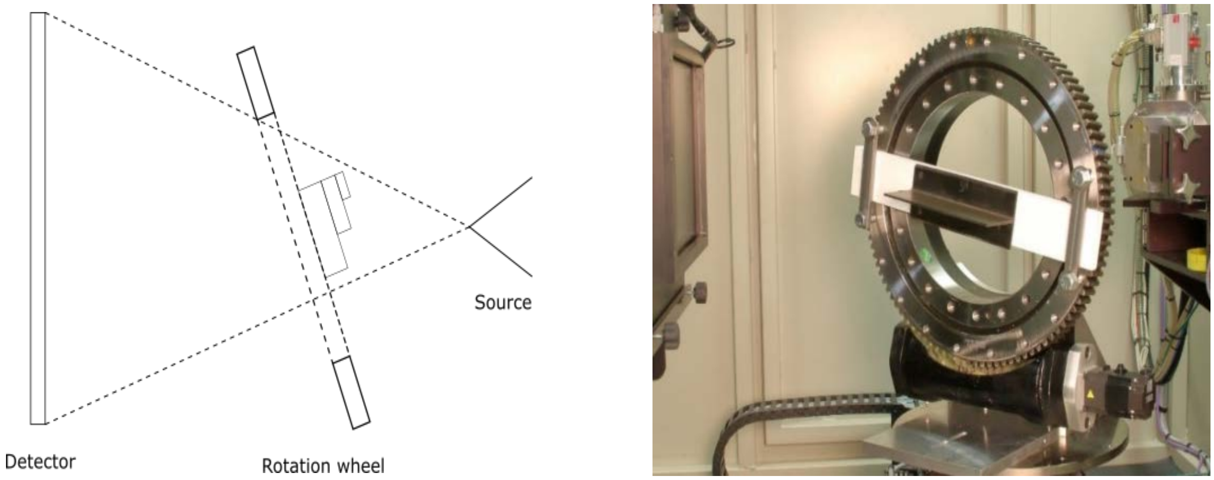

Fig. 21. Inclined CT setup with an inclined wheel, top view (left); wheel device used to perform inclined CT scans (right).

Inclined CT Calibration

Because the axis of rotation is now tilted, the 3D calibration of the scan geometry based on the vertical rotation axis, is not valid anymore. While the cabinet system software does not include an option to calibrate an inclined setup, our reconstruction algorithm explicitly supports this architecture and uses the tilt axis. Note that we also performed a “constructor” calibration, which does not account for the tilt resulting in atypical parameters that led to skewed reconstruction.

We developed a calibration procedure that, in addition to other parameters, measures the tilt angle of the rotation axis, not accessible by the cabinet system 3D calibration. The calibration process consists of minimization of the L2 distance between two sets of 2D points, measured and projected using tilted setup. A set of radiographs is obtained by scanning a known object, usually metallic spheres embedded in a plastic matrix, and a set of features x_{re}, such as sphere centers or corners, are extracted. Using the projection model of the reconstruction, second set of points X_{th} are calculated using known feature locations. The minimization problem can be written as:

$$\{P_k\} = argmin\left(||x_{re} - Proj(X_{th}, \{P_k\})||\right) \quad (18)$$

and can be solved by the Levenberg-Marquardt algorithm [42]. The parameters P_k used in our 3D calibration model are listed in Table 3.

Table 3. Geometry parameters used in the tilted setup and values for the phantom specimen.

SDD	Source-detector distance	896.17 mm
SOD	Source-object Distance	277.78 mm
θ	Tilt Angle	22.26 deg
Offset X	Projection of the center of the volume along the horizontal axis	132.84 mm
Offset Y	Projection of the center of the volume along the vertical axis	136.63 mm

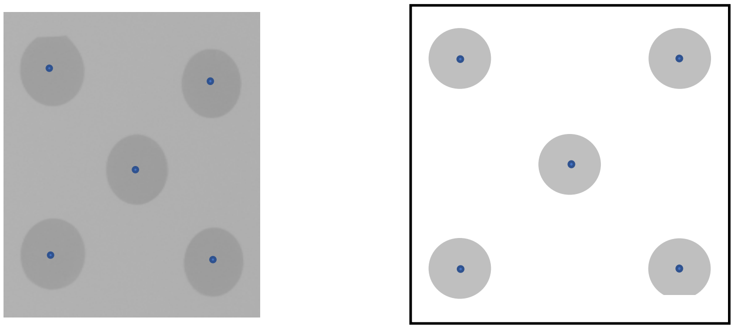

Fig. 2223. Radiograph of the calibration target, the blue dots indicate the extracted features (left); Corresponding theoretical positions of the features (right).

For convenience, all the calibrations were performed using a planar target for the inclined CT setup shown in Fig. 19.

Inclined Setup Effects on the Reconstruction

The main objective of the inclined CT in our case is the detection of 3D defects in large structures. While it may not be possible to achieve a perfect reconstruction of defects because of the lack of information in the radiographs, our goal is to identify problems in using Inclined CT and implement solutions to reduce and mitigate these problems to enable detection of 3D defects.

Due to the inclined geometry and one-sided scan, the available information from radiographs is not complete in the inclined setup, unlike standard CT. A significant amount of work illustrated both theoretically [40, 43-44] and experimentally [45] that the expected reconstruction in an inclined setup presents artifacts. While the sheer amount of data in the radiographs might be the same in inclined scans, its spread and localization is limited due to a specific scan trajectory. The most visible artifact in an inclined reconstruction are parallel streaks, which propagate in the out-of-plane direction of the reconstruction [43].

Computational Phantom

To illustrate these effects, we performed reconstructions using a simulated phantom composed of a single material, shown in Fig.24. The phantom consists of three blocks of decreasing size piled together with circular holes in between them. A few small holes are also drilled on the top of the phantom. We generated a set of 360 noise-free projections using both a standard CT and an inclined CT trajectory with a 60° tilt angle. For reference, the CT reconstruction using a vertical axis setup is shown in Fig. 20.

The reconstruction using an FDK algorithm with Inclined CT geometry is shown in Fig. 26. While the full reconstruction shows a very good agreement with the phantom, the inclined reconstruction lacks contrast. The defects (large holes inside the phantom) are well defined in plane but the out-of-plane image does not recover the shape. The thickness of the defect is difficult to estimate due to the reconstruction artifacts and the cone-shaped streaks in the image. The outer shape is also poorly captured.

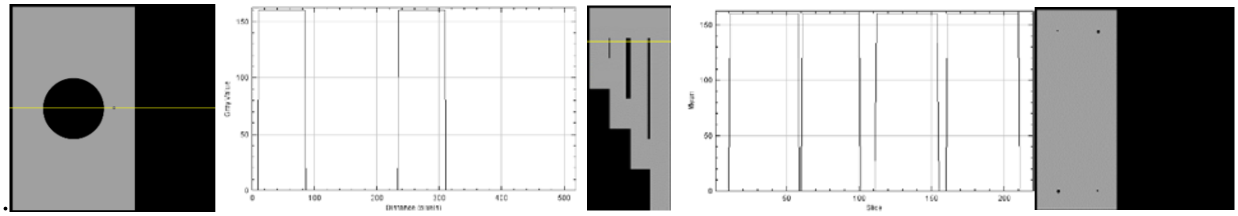

Fig. 24. Phantom profile at different depth and plane.

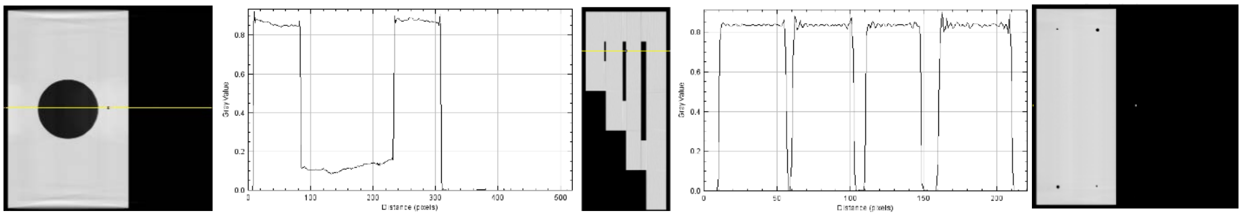

Fig. 25. Full CT reconstruction using a PWLS algorithm.

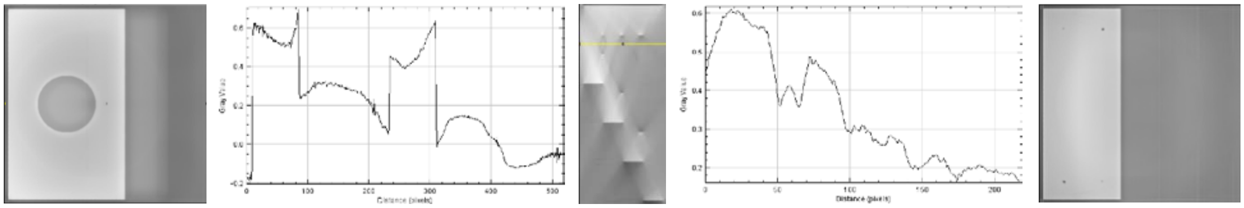

Fig. 26. Inclined CT reconstruction using an FDK algorithm.

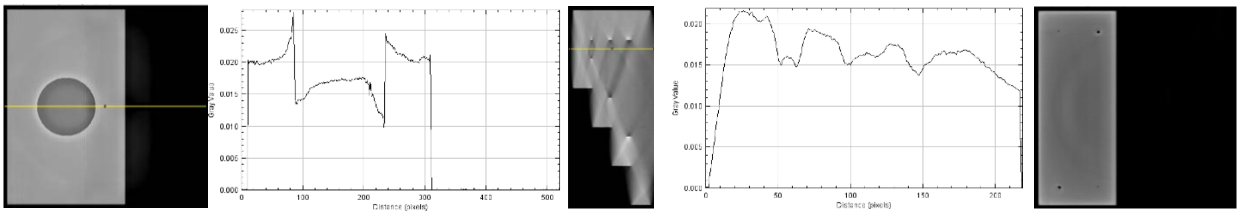

Fig. 27. Inclined CT reconstruction using a PWLS algorithm.

We also performed a reconstruction using the PWLS method as shown in Fig. 27. The iterative reconstruction provides better contrast. The cone-like artifacts are significantly reduced (but still visible) and the outer shape is also more accurate.

Fig. 28 shows the side views of the reconstruction of the holes drilled on the top of the phantom. The Full CT provides an almost perfect reconstruction, while both Inclined CT reconstructions contain streak artifacts. The outer boundaries of the FDK reconstruction cannot be distinguished and thus the drilled holes appear to be inside the material although they are not. This effect is much less pronounced in the PWLS case and the outer boundaries are much closer to the expected ones.

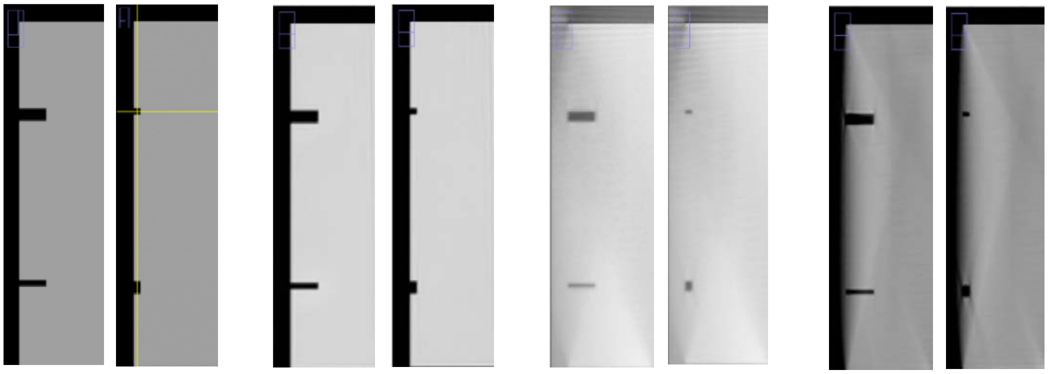

Fig. 28. Reconstruction of the holes of the phantom with several algorithm. From left to right: Phantom, PWLS Full CT, FDK Inclined CT, PWLS Inclined CT.

Defect-Detection Validation Specimen

A real scan can be very different from a computational phantom; and the previous example does not contain either noise, calibration error, misalignments of any kind and it meant to give an idea of the issues that arise in Inclined CT using a seemingly perfect problem. An Aluminum specimen, similar to the computational phantom presented in Section 3.1, was manufactured to test method capabilities. The specimen is composed of 3 blocks separated by a slotted hole acting as a defect instead of circular holes previously used. This specimen was scanned using the tilted table configuration. The calibration parameters are provided in Table 3. The results of an FDK and a PWLS reconstructions are shown in Figs. 29-30.

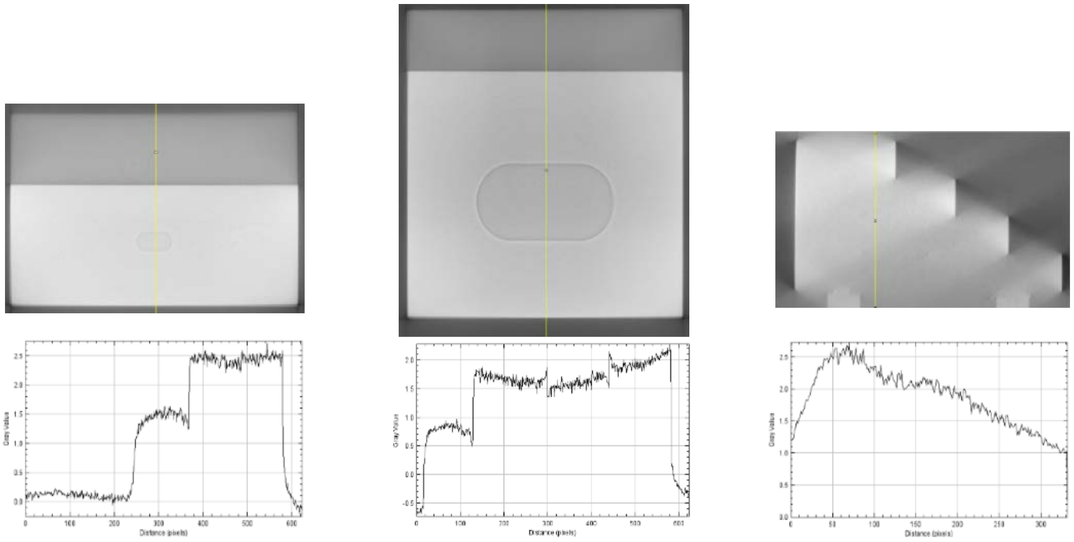

Fig. 29. Inclined CT reconstruction of the phantom specimen using FDK. Top row: in-plane section of small-sized defect (left); large-sized defect (center); side section of middle slice (right). Bottom row: corresponding intensity profiles.

The quality of the reconstruction is noticeably worse than in a perfect phantom case. The bulk of the specimen is inhomogeneous, and the shape boundaries are inconsistent. Part of this behavior can be imputed to the overall noise in the radiographs, not present in the phantom case. In the PWLS case, most of the contrast and overall intensity issues are due to a region of interest problem (see below the complete section on this problem). Unlike a standard scan, the support of the specimen is always present in the trajectory of the beams. The radiographs then contain not only the specimen but also a significant part of the support, which pollutes the data with the extraneous signal.

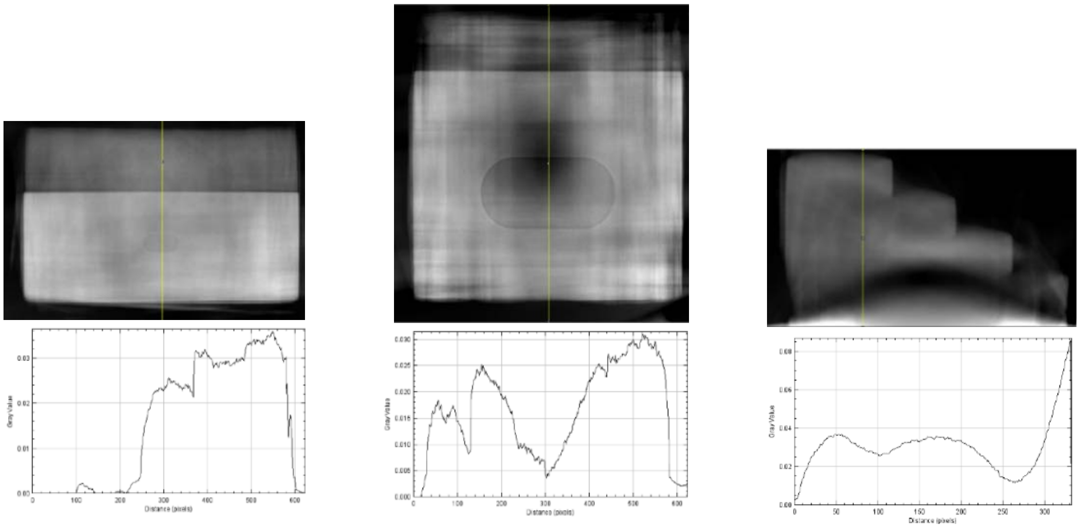

Fig. 30. Inclined CT reconstruction of phantom specimen using PWLS. Top row: in-plane section of small-sized defect (left); large-sized defect (center); side section of middle slice (right). Bottom row: corresponding intensity profiles.

The voids, which is our main interest in the reconstruction, are also significantly more difficult to distinguish on these reconstructions, especially in the PWLS case. The smallest void is almost invisible due to the poor contrast. It can be noted that the cone-shaped streaks are more pronounced in the FDK reconstruction, while the in-plane image seems more granular and noisier.

Thick-Adherend Specimen

In order to better illustrate the differences between the two methods, we used another specimen, whose support did not appear in the radiographs (see Fig. 31, left). This Thick-Adherend specimen is composed of two laminates of Hexcel IM7/8552 Carbon/Epoxy composite bonded together and referred to as TAI8-8. Identifying debonding defects (cracks in the bond) is the main interest of this reconstruction. The scan was performed using the inclined wheel setup.

Overall, reconstructions from Inclined CT (shown in Fig. 32) exhibit significant number of issues. The boundaries are not clearly defined in most cases, due to the incomplete projection data. The FDK and PWLS reconstructions both show large number of artifacts. In the FDK case, the out-of-plane boundaries are not properly identified, but the plane of the defect can still be distinguished. In the PWLS case, the boundaries look better, especially the indents. The streak artifact in the FDK reconstruction is also more pronounced. In plane, the two reconstructions are relatively close, both showing the crack and a significant amount of details, especially the difference between bonded and de-bonded parts. It is important to note that while providing plenty of details and seemingly being sharper, the FDK reconstruction suffers from a defocusing artifact. The specimen is indeed not perfectly aligned out-of-plane and the left and right part of the crack should not be visible at the same time, as can be seen in the PWLS reconstruction. The resulting image contains the sum of several planes instead of the expected sharp image. This effect is also present in the PWLS reconstruction but with a significantly lower intensity. The crack identified in Fig. 31 cannot be distinguished in the FDK reconstruction but can be barely seen in the PWLS. As a result, FDK reconstruction does not result in the same fidelity.

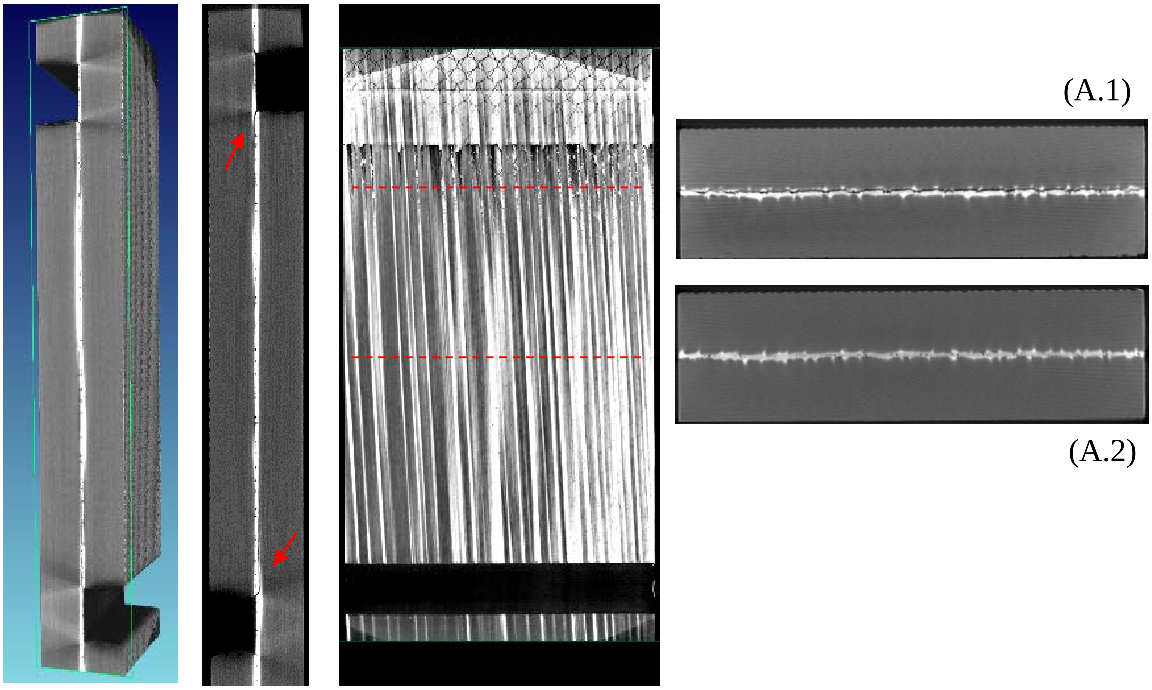

Fig. 31. Full CT reconstruction of the TAI8-8 specimen. From left to right: 3D view, side section slice, in-plane section slice, and top section slices corresponding to the dotted line A.1 and A.2. The crack can be clearly seen in the top cross-section and is not present in the bottom one. Crack locations are identified in the side view by the red arrows.

While in some cases the Inclined CT is used to overcome a geometrical problem such as dimension of the specimen or length ratios, the inclination angle is usually flexible. With our wheel setup, performing a non-inclined scan would be similar to a radiographic scan, almost purely 2D whereas a scan from a 60-degree angle is closer to a standard tomography [27]. Combining information coming from different points of view could improve the reconstruction. As mentioned in the geometry section, our setup is in fact limited for multi-angle scanning since small and large angle scans involve a completely different architecture. It should be noted that since the calibration is performed independently, combining the two geometries is prone to alignment errors [27].

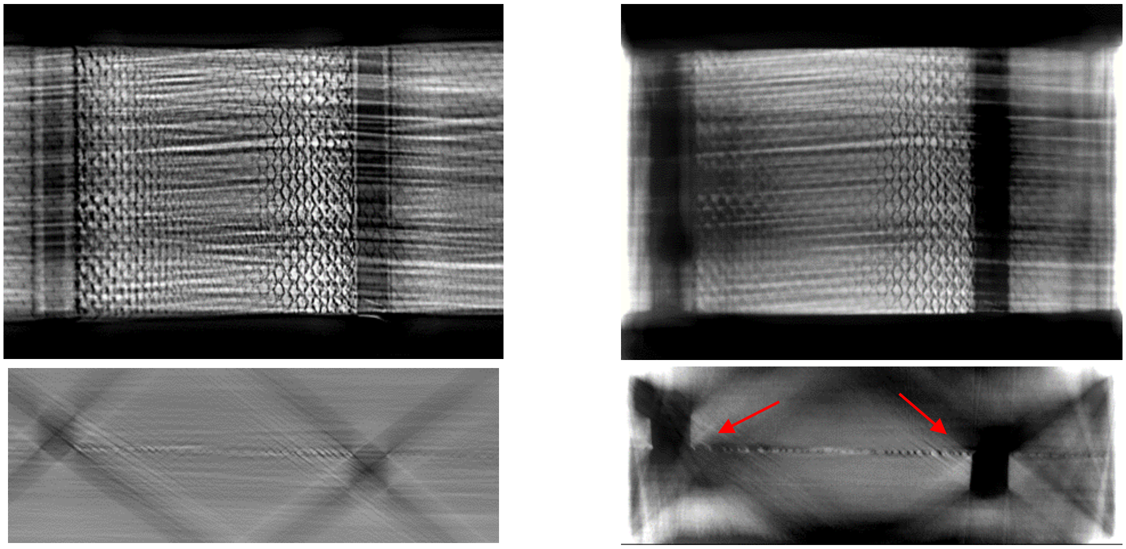

Fig. 32. In-plane sections (top), side sections (bottom) of the inclined CT reconstruction of TAI8-8 specimen (tilt 55° degrees) using FDK (left) and PWLS (right). The debonding defect is indicated by the red arrows and can be seen on the bottom slices.

Improvements to Inclined Reconstructions

We have presented the main issues arising in Inclined CT reconstructions and the differences in quality with full CT by testing the methods on both a numerical phantom and several specimens. While the phantom reconstructions are satisfactory in terms of the defect visibility, the reconstructions performed on real X-ray CT scans showed how noise and the region-of-interest problem impact the quality of the reconstruction and the ability to identify defects. In this section we present the modifications that we used to improve our ability to detect defects.

Reconstruction of Region of Interest

Reconstruction results presented in previous section for the phantom specimen and especially for the TAI8-8 specimen show significant artifacts that appear as a result of Inclined CT reconstruction. However, it turns out that some of the worst artifacts in real scans are actually a result of truncated projection data due to extra material present in radiographs but not included in the reconstructed volume. In case of TAI8-8 specimen, the specimen fixture that is projected only in the region of angles exacerbates this problem. This section demonstrates the modification to iterative algorithms that significantly reduce the artifacts from truncated data.

Reconstruction of region of interest (ROI) volume from a set of truncated projections data is a known problem especially for the iterative reconstruction methods, including the full CT reconstructions. The reason for that is a persistent bias that is added at each iteration and that cannot be compensated only by minimization of the error since forward projections underestimate measured projections. This results in adding artificial high-density features at the edges of reconstructed ROI, which results both in lack of contrast and streaking artifacts. In author's experience the ROI problem applies to all iterative reconstruction methods with varying degree of artifact severity for different methods. In the Inclined CT, reconstruction of ROI is not only an efficiency issue but part of a regular specimen setup since the FOV typically covers only portion of a large specimen. Thus, since analytical algorithms are not optimal for the Inclined CT due to incorrect representation of system geometry, an efficient solution of ROI problem is necessary for the practical implementation of iterative reconstruction for the Inclined CT.

The ROI problem for iterative reconstructions has been addressed in recent research works. Ref. [46] proposed three different techniques: a multi-resolution technique where outside of the ROI volume is reconstructed with lower resolution, and two other techniques based on combination with reconstruction of the full FOV by analytical methods. Ref. [47] proposed a re-projection technique that uses the radiographs with extra material removed using the re-projected radiographs of the full FOV with zeroed ROI. Ref. [48] proposed ray length correction method for SART reconstruction based on *a priori* knowledge of the entire specimen shape. In this work we present the results of two methods that we found as best performing: a) re-projection technique from [47] and b) author's modification of the method from [48] that does not require *a priori* knowledge and applied to the PWLS method.

The re-projection technique [47] proceeds as follows. We will use the sinograms of the 3D phantom presented in the previous section as an illustration for the ROI correction algorithm. The original sinogram is shown in Fig. 33, left. The sinograms are shown logged, hence the specimen appears white. The middle part of the image is the projection of the specimen while the bottom is the projection of the support we used to maintain the specimen. The ROI correction consists in performing a fast pre-reconstruction of larger volume using FDK or PWLS with typically smaller resolution, zeroing the ROI volume within the reconstructed volume, and then removing the projections of the updated volume from the original projections. An example of the corrected sinogram is shown Fig. 33, right. This is the difference between the original sinogram and the re-projection of the fast reconstruction mention above.

Fig. 33. Sinograms of the real phantom use in the Region of Interest correction. Original sinogram (left), re-projection (middle), difference (right).

Re-projected correction in Fig. 33, middle should contain only the projection of the unwanted part of the complete projection area: in this case, the re-projected projections only contain the support of the specimen that does not need to be reconstructed. This correction is then removed from the original projections, and the updated projections are used in the reconstruction algorithm.

The impact of ROI correction on the ICT reconstruction is very important as can be seen in Fig. 34. The quality of geometry estimation is improved using a ROI correction in the PWLS case. The main difference comes from the rebalance of the intensity within the reconstruction. It can be seen on the PWLS reconstruction that while there was a concentration of the intensity in the middle of the specimen and a lack of it in the bottom, the intensity is redistributed in the ROI-corrected reconstruction. This correction has no effect on the FDK reconstruction and the results of Fig. 29 were not improved any further.

It should be noted that while the overall quality has improved, the visibility of the defects from the side views of the reconstruction is still very limited. All the defects, even the smallest one, are visible and not obscured by artifacts in the in-plane sections, but still almost invisible in the side views. The figures demonstrate much better reconstruction contrast as compared to no-ROI correction case. In fact, improvements to contrast and reduction of border artifacts significantly outperform deficiencies due to solution shift.

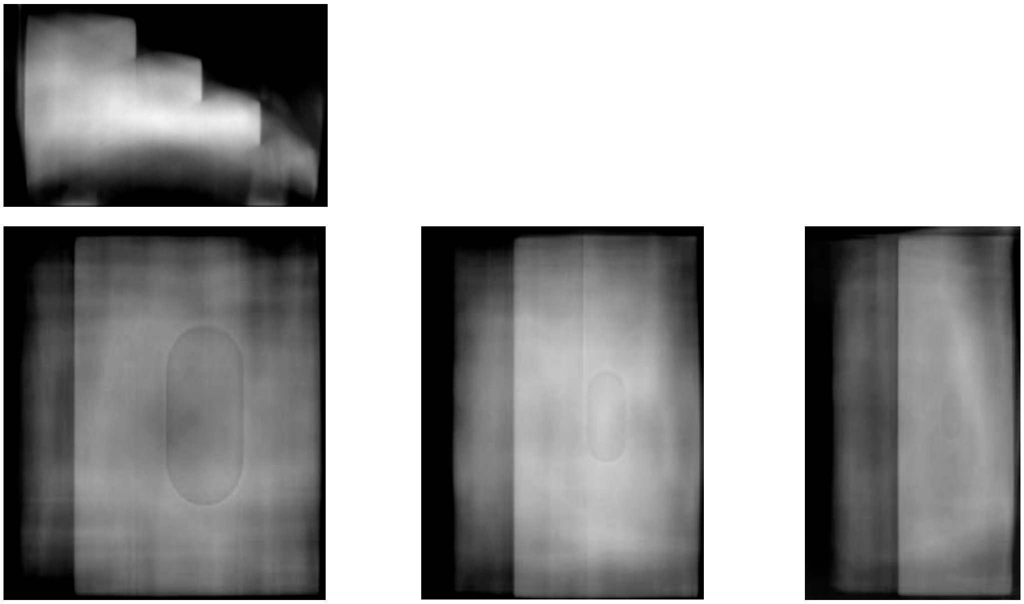

Fig. 34. ROI-corrected reconstruction of the phantom specimen using PWLS.

The second ROI correction method described in this work is a modification of [48]. In the original proposal, the iterative update of the SART method was modified to use true, *a priori* known ray lengths through the entire specimen for each pixel on the detector. In the update law, the projection operators were scaled to global ray length by dividing them by $k_i^{ROI} = \frac{\sum_j A_{ij}}{l_i^G}$, and backprojections were multiplied by k_i^{ROI}. In practice, finding l_i^G is not trivial, and to simplify the application of this correction, we propose to use fixed "true" value of $l_i^G = l_f$ for all rays. This update essentially favors the internal ROI rays as opposed to rays that cross small portions of ROI volume, which reduces the ROI artifacts. One could immediately notice that, in contrast with the method in [48], this update formula technically leads to modified solution since projections are scaled by factors not substantiated by the actual geometry. However, we found the solution discrepancy is typically small and exhibited only by decreased density in the center of the volume, while ROI artifacts are significantly decreased, which still makes this method attractive due to simplicity. The value of l_f can be typically selected as the approximate size of the FOV.

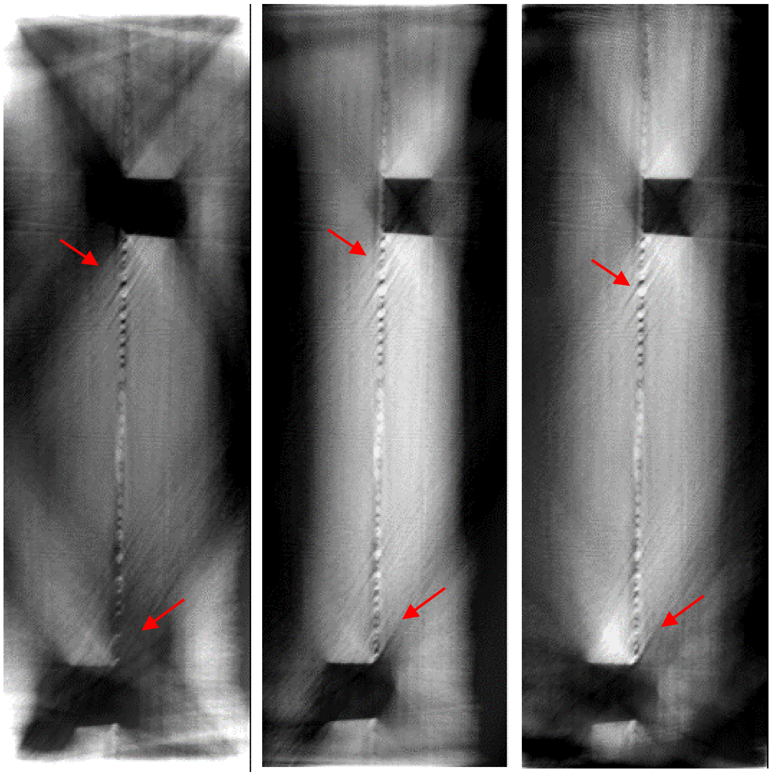

Fig. 35. Side sections of the PWLS reconstruction of the TAI8-8 specimen. From left to right: No ROI, reprojection method, fixed length method. The debonding defect is indicated by the red arrows.

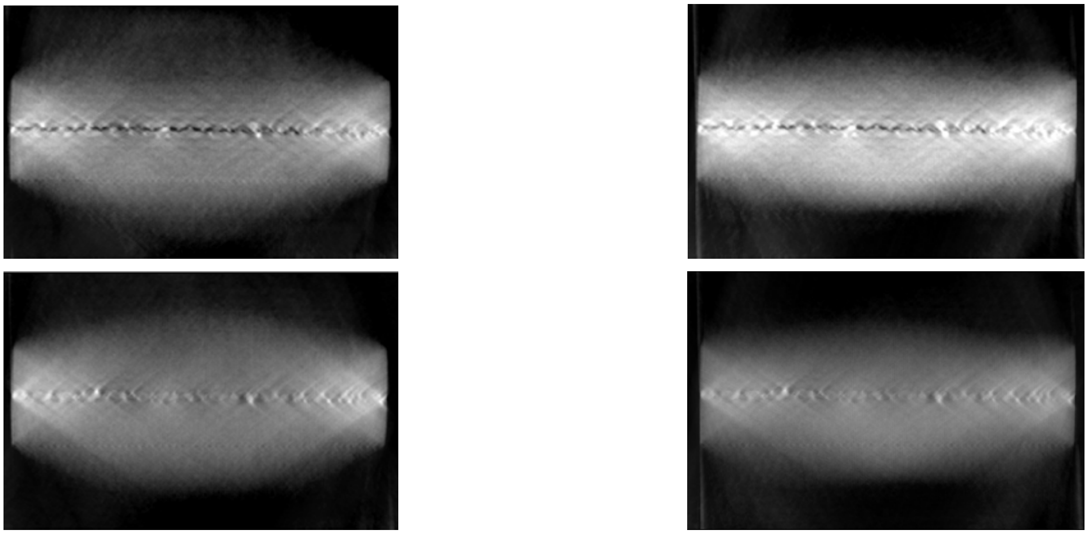

Fig. 36. Top section A.1 (top), A.2 (bottom) from Fig. 31 of the PWLS reconstruction of the TAI8-8 specimen using reprojection method (left) and fixed length method (right).

Figs. 30-31 show comparison of PWLS reconstruction for the TAI8-8 specimen using no ROI correction, re-projection ROI, and fixed ray length ROI. Side sections and top sections A.1 and A.2 defined in Fig. 31 are shown. The contrast and the outer boundaries are made clearer by the correction. The bonding is visible in all cases, but we can notice that using ROI correction improves the quality of reconstruction by a significant margin. The crack is visible on slice A.1 and not on slice A.2 (as in the full CT reconstruction) in all cases but the reconstruction in finer in the corrected reconstruction. However, as compared with the re-projection method, the fixed length method presents lower quality solution both in terms of reconstructed specimen shape and in severity of artifacts. But keep in mind that the advantage of this method is its simplicity and very fast performance that matches the original algorithm.

Priors

One of the advantages of using iterative methods to solve the reconstruction problem is the opportunity to add *a priori* information or some knowledge about the solution. The solution can be weakly enforced to satisfy certain properties. The regularity of the reconstruction can thus be controlled (in a weak sense) by penalizing the solution while solving the optimization problem. One of the classical regularization functions is the Total-Variation penalty, which can be written as an additive term computed from the gradient of the volume [49]. The iterative reconstruction problem then becomes:

$$x_{sol} = \text{argmin } |Ax - y|^2 + \eta \|x\|_{reg} \tag{19}$$

The regularization function we choose to use is composed of the two terms. The first part is a simple Tikhonov penalty while the second part is a hyperbola function approximating the typical TV function, effectively replacing the typical L1-norm of the gradient by a more regular function.

The Tikhonov regularization within the PWLS algorithm is used to avoid ill-conditioned behavior of projection/backprojection operators. This regularization tends to remove large intensity peaks in the reconstruction, accompanied by a smoothing effect. While limiting the intensity peak improves the quality of the reconstruction, the loss of sharpness is detrimental to the identification of the defects or the other features of the specimen.

The hyperbolic TV regularization aims at improving the reconstruction in the context of lack of data. This function favors penalizing small gradients in the reconstruction, effectively making the term an edge-preserving prior. The solution should be led towards the lowest gradient values while keeping the edges and features of the specimen as sharp as possible.

Fig. 38 shows compares the reconstruction of the TAI8-8 specimen with and without hyperbolic regularization. The TV reconstruction provides a significantly cleaner image, as the amount of noise is reduced in the reconstruction. The image also looks less sharp, as the edges are smoothed by the Hyperbolic function but the debonding is still clearly visible. It should be noted that small artifacts may be erased by the inherent smoothing of the prior if its influence in the optimization principle outweighs the solution error.

Bilateral Filtering

In addition to using priors, quality of the reconstruction can also be improved using filters tailored to target specific issues in the volume. In our case, scan and specimen geometry allow us to consider 2D in-plane slices independently as their reconstruction has superior accuracy compared to thickness slices. By filtering each slice in the volume, the overall quality can be improved, and the memory footprint of the process can be kept relatively small.

A suitable filter should act as an averaging filter, to reduce the noise and flatten the gradients inside a homogeneous area but would not impact large gradients or disparities in intensity. Non-local filtering has been used in image reconstruction; in tomosynthesis, non-local means (NLM) filtering based on similarity of neighboring pixels has been proposed to improve slice blur [50]. We selected the bilateral filter [51-52] among the available filters due to its simplicity . This filter is a convolution composed of a spatial and a range component:

$$O(p) = \sum_{q\in\Omega_s} \Big(G_s(\|p-q\|)\, G_r\big(\|I_p - I_q\|\big)\Big)\, I(p) \tag{20}$$

where G_s and G_r are Gaussian kernels. The first one is a spatial Gaussian filter acting as an averaging filter. The second filter is a range filter, whose argument is the intensity of a pixel and not its position, which effectively penalizes pixels that have values different from the one in the kernel. The principle of such a filter is shown in Fig. 37.

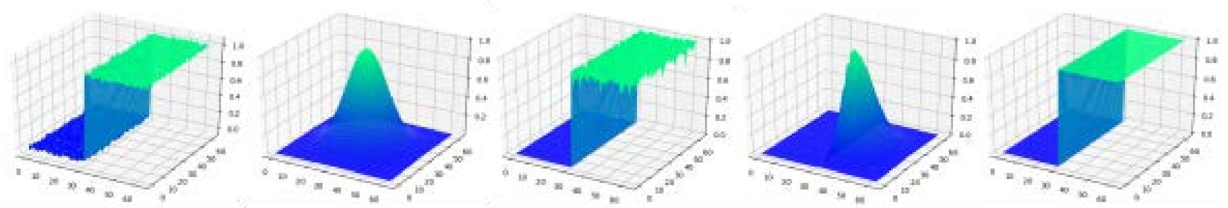

input

spatial kernel

intensity kernel for the central pixel

weight of the filter for the central pixel

output

Fig. 37. Principle of the Bilateral filter [51].

While it is very efficient against noise, a one-pass filter may not be sufficient to remove some of the smoothest disparities, *i.e.* low frequency intensity variations, but implementing a multi-pass filter may improve this behavior. It was not implemented in this work as the it requires high computational cost.

Computational efficiency of a convolution strongly depends on the implementation and both computational power and memory available. It should be noted that the extension of this filter to 3D volume could be used but we chose to filter each 2D image independently for practical reasons. The kernel size of the range filter acts as a high pass filter on the intensity difference. This means that any jump in intensity greater than around three times than the kernel size will be averaged and ultimately removed.

The kernel size is case-dependent and has to be chosen empirically since it is a compromise between the noise level and the accuracy of the reconstruction. In order to make it more automatic, and remove the case dependency, we propose a variance-based kernel size. Instead of selecting one range kernel for the entirety of the slice, the value is computed for each window independently as a function of the variance. As a result, when a window should contain only one intensity level its variance is driven by the noise level and the filter acts accordingly. If a window contains an edge, its variance will change, but will always stay in between the noise level and the material intensity jump. It allows to always select the largest size in between these two scales. It should be noted that if the noise level is similar to the jump in intensity, such as for a small defect in a noisy reconstruction, this process is likely to filter the defect out of the image. In some cases, the bilateral filter may create a “staircase effect” [53], which is detrimental to the reconstruction.

Fig. 38 shows the reconstruction by PWLS algorithm followed by a bilateral filtering using a 5-by-5 window and variance-based kernel size. The level of noise is dramatically reduced at the expense of a visibly altered image. The features of the specimen are clearly visible and the debonding can be clearly distinguished. The crack is not as well defined as in Fig. 31 but filtering small variations from the reconstruction makes it easier to see its effects, especially on the bonding pattern. Total variation introduces a significant amount of blur, which is not suitable for our purpose. On the contrary, bilateral filtering makes the debonding defect clear for slice A.1 and reduces the number of artifacts for slice A.2.

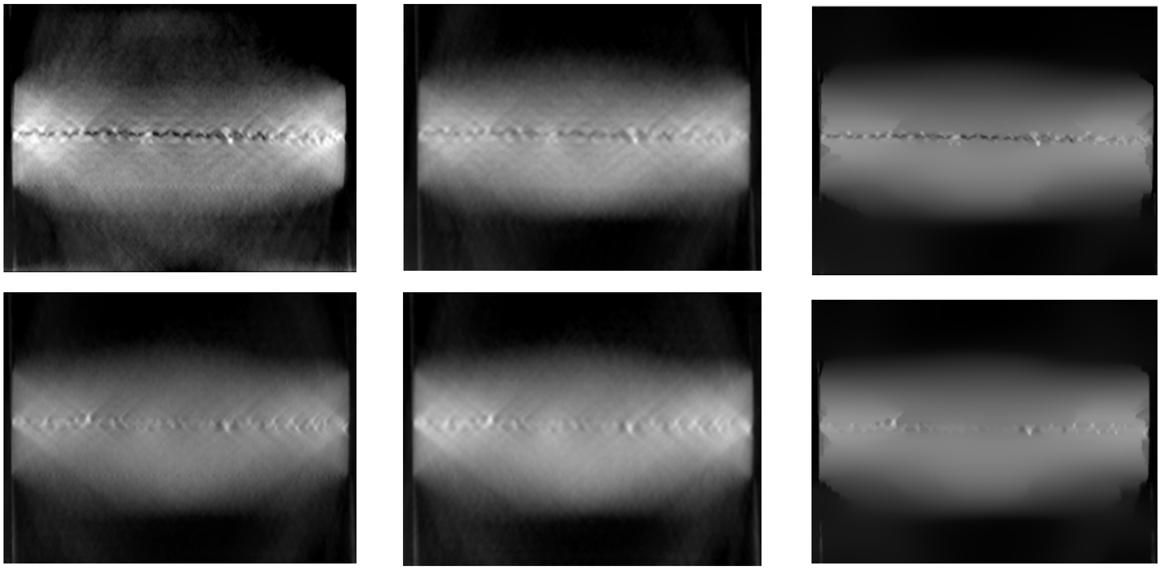

Fig. 38. Section A.1 (top), section A.2 (bottom) from Fig. 31; PWLS reconstruction of the TAI8-8 specimen with No regularization (left), TV regularization (center), Bilateral filtering inside the de-bonded section (right).

For comparison, Fig. 39 shows the reconstruction using a 15x15 window for the filtering. The overall effect is similar to the 5x5 window, the noise is filtered but the debonding defect is clearer. Using large spatial kernels is impractical in large volumes without a very efficient implementation. However, using even a 5x5 filter leads to a significant improvement in clarity of the reconstruction and visibility of the crack.

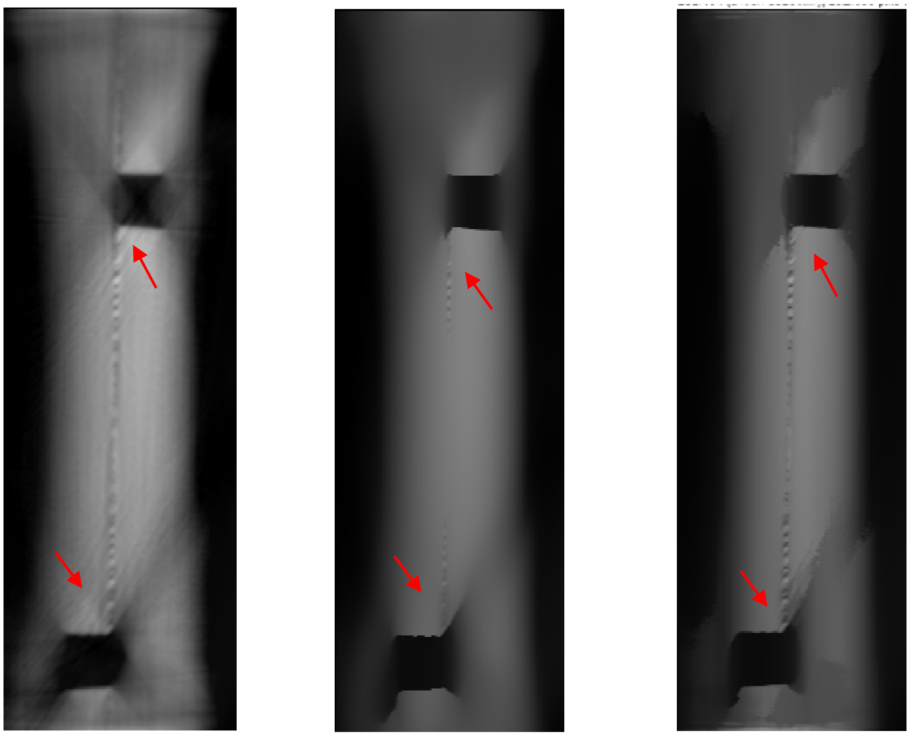

Fig. 39. Side sections of the PWLS reconstruction of the TAI8-8 specimen using TV regularization (left), Bilateral filtering 5x5 kernel (center), Bilateral filtering 15x15 kernel (right). Debonding defects are indicated by the red arrows.

Inclined Computed Tomography for Large Structures

Tomography setups and reconstruction methods described in previous sections lead the way to development of 3D inspection capability for large structures. AMSL has been developing game-changing CT technologies breaking through the inspection object size limitation of computed tomography. The CT system is designed such that the nondestructive inspection is conducted on a single side of the component allowing for the unlimited in-plane dimensions. This technology allows for effective inspection of critical areas including bonded joints in large structures at micron-scale resolution.

Fig. 40 shows the inspection concept. The specimen is positioned between X-ray source and detector and stays motionless during the scan. X-Ray source is inclined at a large (about 60 degree) angle from vertical axis supported by the arm, which is rotated around the vertical for 360 degrees. On the other side of the specimen, the detector moves accordingly to the position of the source such that the inspected area stays in the field of view. Detector can be made perpendicular to the direction of the source or move horizontally: the latter allows for more workspace and freedom in magnification but requires larger detector displacements. Large inclination angle of the source allows improving 3D resolution of defects through the thickness as shown in this project's developments.

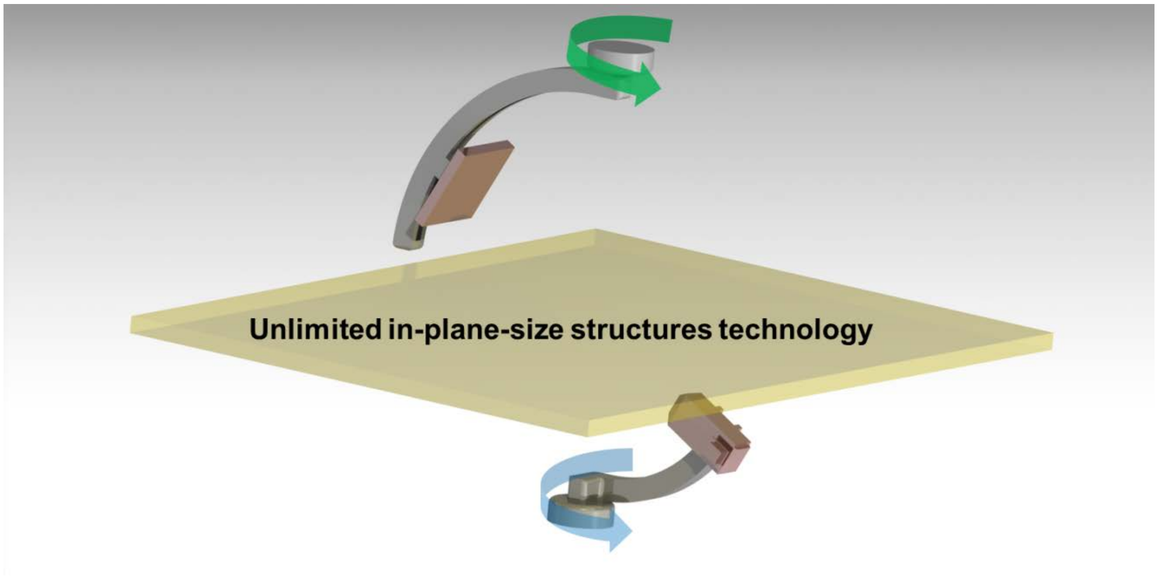

Fig. 40. Rotational stage concept for large structures.

We plan to develop a prototype CT inspection system capable of achieving up to 30-micron resolution scans in up to 35-foot-long structures. It is worth noting that using CT for detection of defects in large structures may require analyzing high-resolution projection data and very large solution volumes. In this project we developed a high-performance CT reconstruction capability for efficiently running such analysis, which is based on high-performance GPGPU implementation combined with fast convergence methods necessary for applying iterative algorithms in practical situations. The prototype should demonstrate performance of the proposed inspection setup and reconstruction methods to identify critical defects in the full-sized aerospace structures that currently lack such inspection capability.

References

[1] Makeev A, Seon G, Nikishkov Y, Nguyen D, Mathews P, Robeson M. Analysis Methods Improving Confidence in Material Qualification for Laminated Composites, *Best Paper Award , Structures and Materials, 72nd American Helicopter Society Forum*, West Palm Beach, Florida, May 17-19, 2016.

[2] Makeev A, Seon G, Nikishkov Y, Lee E. Methods for Assessment of Interlaminar Tensile Strength of Composite Materials, *Journal of Composite Materials*, 2015;49:783-794.

[3] Seon G, Makeev A, Nikishkov Y, Lee E. Effects of Defects on Interlaminar Tensile Fatigue Behavior of Carbon/Epoxy Composites, *Composites Science and Technology*, 2013;89: 194-201.

[4] Nikishkov, Y., Bostaph, E., Makeev, A. Detection of Defects in Composites by Limited-Angle Tomography, *Proceedings of the American Society for Composites 29th Technical Conference*, San Diego, California, September 2014.

[5] Nikishkov Y, Bostaph E, Makeev A. Nondestructive Inspection of Composite Structures based on Limited Angle X-ray Computed Tomography, *Proceedings of the American Helicopter Society 71st Annual Forum*, Virginia Beach, VA, May 5-7, 2015.

[6] Kalender WA, Computed tomography, Publicis Publishing, Erlangen, 2011.
[7] Nikishkov Y, Airoldi L, Makeev A. Measurement of voids in composites by X-ray computed tomography. Compos Sci Technol 2013;89:89–97.
[8] Radon, J. On the determination of functions from their integral values along certain manifolds. *IEEE Transactions on Medical Imaging*. 1986;5(4):170–176.
[9] Feldkamp LA, Davis LC, Kress JW. Practical cone-beam algorithm. Opt Soc Am 1984;1:612–9.
[10] Kak AC, Slaney M. Principles of computerized tomographic imaging. New York, NY: IEEE Press; 1988.
[11] SciPy.org. numpy.fft.fftshift, https://docs.scipy.org/doc/numpy-1.15.0/reference/generated/numpy.fft.fftshift.html; 2019 [accessed 13 December 2019].
[12] Moisan L. Periodic plus smooth image decomposition. J Math Imaging Vis 2011;39:161–79. doi:10.1007/s10851-010-0227-1.
[13] De Man B, Basu S. Distance-driven projection and backprojection in three dimensions. Phys Med Biol 2004;49:2463–75. doi:10.1088/0031-9155/49/11/024.
[14] Long Y, Fessler JA, Balter JM. 3D forward and back-projection for X-ray CT using separable footprints. IEEE Trans Med Imaging 2010;29:1839–50.
[15] Gordon R, Bender R, Herman GT. Algebraic reconstruction techniques (ART) for three-dimensional electron microscopy and X-ray photography. J Theor Biol 1970;29:471-81.
[16] Fessler JA. Statistical image reconstruction methods for transmission tomography. In: Sonka M, Fitzpatrick MJ, editors. Handbook of medical imaging, vol 2. Medical image processing and analysis, SPIE Publications, 2000, p. 1-70.
[17] Hudson HM, Larkin RS. Accelerated image reconstruction using ordered subsets of projection data. IEEE T Med Imaging 1994;13(4):601-6.
[18] Andersen A, Kak A. Simultaneous algebraic reconstruction technique (SART): a superior implementation of the ART algorithm. Ultrason Imaging 1984;6(1):81–94.
[19] Elbakri A, Fessler JA. Statistical image reconstruction for polyenergetic X-ray computed tomography. IEEE T Med Imaging 2002;21(2):89-99.
[20] Gregor J, Fessler JA. Comparison of SIRT and SQS for regularized weighted least squares image reconstruction. IEEE T Comput Imaging 2015;1(1):44-55.
[21] van Aarle W, Palenstijn WJ, Cant J, Janssens E, Bleichrodt F, Dabravolski A, et al. Fast and flexible X-ray tomography using the ASTRA toolbox. Opt Express 2016;24:25129.
[22] Penßel C, Kalender WA, Kachelrieß M. ROI-Driven CT Trajectories. 2006 IEEE Nucl Sci Symp Conf Rec, San Diego, CA, USA: 2006, p. 1969–72.
[23] Dabravolski A, Batenburg KJ, Sijbers J. Adaptive zooming in X-ray computed tomography. J Xray Sci Technol 2014;22:77–89. doi:10.3233/XST-130410.
[24] Maaß C, Knaup M, Kachelrie M. New approaches to region of interest computed tomography. Phys Med 2011;38:2868–78. doi:10.1118/1.3583696.
[25] Kyrieleis A, Titarenko V, Ibison M, Connolley T, Withers PJ. Region-of-interest tomography using filtered backprojection: assessing the practical limits. J Microsc 2011;241:69–82.
[26] Zhou J, Maisl M, Reiter H, Arnold W. Computed laminography for materials testing. Appl Phys Lett 1996;68:3500–2.
[27] Fisher SL, Holmes DJ, Jørgensen JS, Gajjar P, Behnsen J, Lionheart WRB, Withers PJ. Laminography in the lab: imaging planar objects using a conventional x-ray CT scanner. Meas Sci Technol 2019;30:1–13.

[28] Xu F, Helfen L, Baumbach T, Suhonen H. Comparison of image quality in computed laminography and tomography. Opt Soc Am 2012;20:361–6.

[29] Helfen L, Myagotin A, Rack A, Pernot P, Mikulík P, Di Michiel M, Baumbach T. Synchrotron-radiation computed laminography for high-resolution three-dimensional imaging of flat devices. Phys Status Solidi A Appl Mater Sci 2007;204:2760–5.

[30] Brien NSO, Boardman RP, Sinclair I, Blumensath T. Recent advances in x-ray cone-beam computed laminography. J Xray Sci Technol 2016;24:691–707.

[31] Wood CE, O 'Brien NS, Denysov A, Blumensath T. Computed laminography of CFRP using an X-ray cone beam and robotic sample manipulator systems. IEEE Trans Nucl Sci 2018;67:1384–93. doi:10.1109/tns.2019.2895910.

[32] Nuyts J, De Man B, Fessler JA, Zbijewski W, Beekman FJ. Modelling the physics in the iterative reconstruction for transmission computed tomography. Phys Med Biol 2013;58:R63-96.

[33] Kruth JP, Bartscher M, Carmignato S, Schmitt R, Chiffre L De, Weckenmann A. Computed tomography for dimensional metrology. CIRP Ann - Manuf Technol 2011;60:821–42.

[34] SciPy.org. scipy.optimize.leastsq, docs.scipy.org/doc/scipy/reference/generated/ scipy.optimize.leastsq.html; 2019 [accessed 13 December 2019].

[35] Kraemer A, Kovacheva E, Lanza G. Projection based evaluation of CT image quality in dimensional metrology. Digit. Ind. Radiol. Comput. Tomogr.. 2015, p. 1–10.

[36] Gondrom S, Zhou J, Maisl M, Reiter H, Kröning M, Arnold W. X-ray computed laminography: an approach of computed tomography for applications with limited access. Nucl Eng and Des 1999;190:141-7.

[37] Maisl M, Porsch F, Schorr C. Computed laminography for X-ray inspection of lightweight constructions. In: Proc 2nd Int Symp on NDT in Aerospace, Hamburg, Germany, 2010.

[38] Holub W, Habler U, Schorr C, Maisl M, Janello P, Jahnke P. XXL-Micro-CT comparative evaluation of microscopic computed tomography for macroscopic objects. In: Proc Dig Ind Radiol Comput Tomogr (DIR 2015), Ghent, Belgium, 2015.

[39] Krumm M, Sauerwein C, Hämmerle V, Heile S, Schön T, Jung A et al. Rapid robotic X-ray computed tomography of large assemblies in automotive production. In: Proc. 8th Conf Ind Comput Tomogr (iCT 2018), Wels, Austria, 2018.

[40] Frikel J, Quinto ET. Characterization and reduction of artifacts in limited angle tomography. Inverse Probl 2013;29(12):125007.

[41] Quinto ET. Singularities of the X-ray transform and limited data tomography in R2 and R3. SIAM J Math Anal 1993;24:1215-25.

[42] Marquardt D. An algorithm for least-squares estimation of nonlinear parameters. SIAM J Appl Math 1963; 11:431-41.

[43] Quinto ET. Artifacts and visible singularities in limited data X-ray tomography. Sensing and Imaging 2017;18(9):1-14.

[44] Borg L, Frikel J, Jørgensen JS, Quinto ET. Analyzing reconstruction artifacts from arbitrary incomplete X-ray CT data. SIAM J Imaging Sci 2018;11(4):2786-814.

[45] Xu F, Helfen L, Baumbach T, Suhonen H. Comparison of image quality in computed laminography and tomography. Opt Express 2012;20(2):794-806.

[46] Hsieh J, Thibault JB, Bouman CA, Sauer K. Iterative method for region-of-interest reconstruction. US Patent 6,768,782 B1, 27 July 2004.

[47] Ziegler A, Nielsen T, Grass M. Iterative reconstruction of a region of interest for transmission tomography. Med Phys 2008;35(4):1317-27.

[48] Schorr C, Maisl M. A ray-length-based ROI-correction for computed laminography. In: 5th Conf Ind Comput Tomogr (iCT), Wels, Austria, 2014.

[49] Sidky EY, Pan X. Image reconstruction in circular cone-beam computed tomography by constrained, total-variation minimization. Phys Med Biol 2008;53(17):4777-807.

[50] Ertas M, Yildirim I, Kamasak M, Akan A. An iterative tomosynthesis reconstruction using total variation combined with non-local means filtering. BioMed Eng OnLine 2014;13:65.

[51] Ichikawa K, Kawashima H, Shimada M, Adachi T, Takata T. A three-dimensional cross-directional bilateral filter for edge-preserving noise reduction of low-dose computed tomography images. Comput Biol Med 2019;111:103353.

[52] Tomasi C, Manduchi R. Bilateral filtering for gray and color images. In: Proc 6th Int Conf Computer Vision (ICCV 98), Bombay, India, 1998.

[53] Buades A, Coll B, Morel JM. The staircasing effect in neighborhood filters and its solution. IEEE T Image Process 2006;15(6):1499-505.